Phase-field simulation and coupled criterion link echelon cracks to internal length in antiplane shear

Gergely Molnár, Aurélien Doitrand, Véronique Lazarus

Phase-field simulation and coupled criterion link echelon cracks to internal length in antiplane shear

Gergely Molnár[a,*], Aurélien Doitrand[b], Véronique Lazarus[c]

[a] *CNRS, INSA Lyon, LaMCoS, UMR5259, 69621 Villeurbanne, France*
[b] *Univ Lyon, INSA Lyon, Université Claude Bernard Lyon 1, CNRS, MATEIS, UMR5510, 69621 Villeurbanne, France*
[c] *IMSIA, ENSTA Paris, CNRS, CEA, EDF, Institut Polytechnique de Paris, 828 boulevard des Maréchaux, F-91762 Palaiseau, France*

Abstract

This paper provides a comprehensive numerical analysis of daughter crack localization in pure antiplane shear. Although antiplane shear fracture is important in various industrial applications, understanding the morphology of the resulting fragmentation remains challenging. The paper develops innovative phase-field models to induce the facets using a small spatial variation in the toughness field and examines the impact of numerical and material parameters on the newly formed daughter cracks' shape and spacing. Through meticulous comparison to the coupled criterion, the paper reveals a compelling connection between the internal length-scale of damage regularization, Irwin's length and the facet crack spacing. Furthermore, the effect of Poisson's ratio on the crack form and spacing is investigated: the results reveal a significant influence and showcase comparable initiation distances between the numerical simulations and experimental measurements in pure antiplane loading.

Keywords: Mode III loading, Antiplane shear, Phase-field fracture, Coupled criterion, Internal length, Echelon cracks

1. Introduction

In the context of linear elastic fracture mechanics, loading in the vicinity of a preexisting crack can be decomposed into three loading modes: mode I, corresponding to tensile opening; mode II, corresponding to in-plane shear; and mode III, corresponding to antiplane shear (Irwin, 1958; McClintock and Irwin, 1965). The quantitative understanding of fracture in the presence of mode III loading is relatively obscure compared to mode I+II, primarily due to the complexity and 3D nature of the crack propagation pattern. While propagation in mode I+II generally occurs smoothly and can be addressed through a 2D elasticity problem (Erdogan and Sih, 1963), mode III loading often results in the fragmentation of the crack into numerous facets with complex 3D shapes (Sommer, 1969; Knauss, 1970; Lazarus et al., 2008; Pham and Ravi-Chandar, 2014), making accurate prediction of its morphology challenging.

Mode III fracture is of significant concern in industrial applications, as it can occur in various materials and structures subjected to torsional loading. Examples of such applications include propeller shafts in shipbuilding (Fonte et al., 2006), helicopter and jet engines in the aerospace industry (Raghavachary et al., 1990), automotive components, energy industry

*Corresponding author
Email address: gergely.molnar@insa-lyon.fr (Gergely Molnár)

equipment such as wind turbines and generators (Nikravesh and Meidan-Sharafi, 2016), and even in rails experiencing the passage of train wheels (Bonniot et al., 2018).

In addition to its importance for safety reasons in industry, understanding antiplane shear fracture is also relevant in other areas of science and engineering. For example, the study of this fracture mode can provide valuable insights into the behavior of fractures in earthquakes (Cooke and Pollard, 1996; Cambonie et al., 2019), where shear loading is common. Additionally, in medical science (Zimmermann et al., 2009), spiral fractures in bones are a common type of antiplane shear fracture that requires careful diagnosis and treatment.

Finally, the understanding of antiplane shear fracture can also be applied in the design and fabrication of architected materials (Alsaadi et al., 2018), which are composite materials with designed microstructures to achieve desired mechanical properties. By incorporating knowledge of antiplane shear fracture into the design process, it is possible to create materials that are more resistant to shear loading and thus have improved overall strength and toughness.

The first well-controlled experiments demonstrating crack facet segmentation were conducted by Sommer (1969) using glass. During the same period, Knauss (1970) and later Palaniswamy and Knauss (1978) demonstrated the formation of semi-penny-shaped cracks in pure mode III conditions. Since the 1970s, numerous researchers have shown that the appearance of daughter cracks is independent of the material, segmentation occurs during the movement of tectonic plates (Pollard et al., 1982; Cox and Scholz, 1988), in the orogeny of mountains (Younes and Engelder, 1999), and in solids such as polymers (Hull, 1994; Lazarus et al., 2008; Lin et al., 2010; Chen et al., 2015), gels (Ronsin et al., 2014), gypsum, and even in cheese (Goldstein and Osipenko, 2012).

The characteristic behavior under investigation is depicted in Fig. 1 (Lazarus et al., 2008; Hattali et al., 2021). The initial slit (observable in black) segments into facets or echelon cracks. In the literature, the initial slit is referred to as the "mother

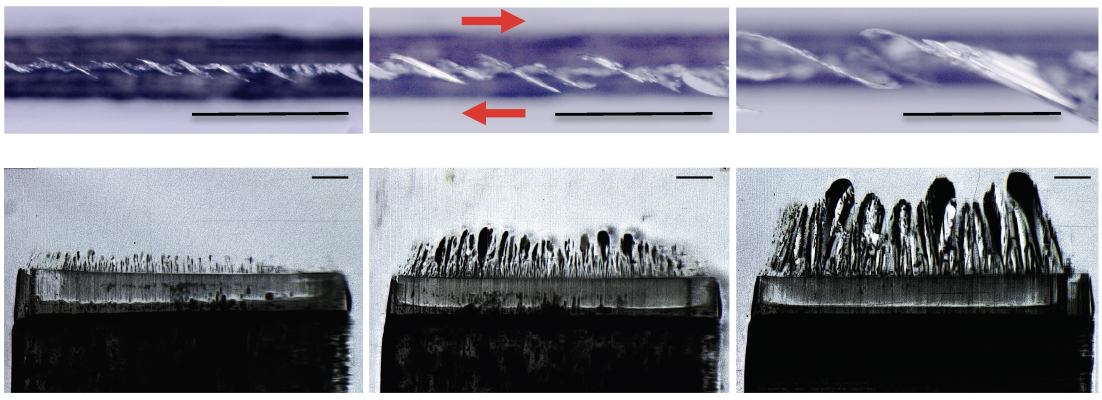

Figure 1: Typical segmentation and facet coarsening observed in fatigue bending experiments performed on plexiglass with an inclined initial crack (Chen et al., 2015; Lazarus et al., 2020; Hattali et al., 2021). The bar in each figure represents 1 mm. The first row shows the sample from the top, with facets advancing in this direction. The initial slit appears dark and blurred in the background, and the facets are clear and sharp in the foreground. The second row shows the view from the side, depicting the crack propagation upwards. Each column represents the advancement in time, illustrating the crack evolution during the experiments.

crack", and the small facets are termed "daughter cracks". These daughter cracks then progressively advance in the direction of the original slit, gradually transforming to obtain a pure mode I opening state. As the crack propagates, the initially small facets grow both in length and width, eventually coalescing and merging into larger and fewer facets. In this paper, we will use both the terminology "facets", "echelon" or "daughter" cracks to describe the segmented crack front.

The mixed mode problem can be addressed at two scales (Leblond et al., 2015; Lazarus et al., 2020). At the macroscopic scale, crack propagation is governed by the principle of local symmetry or the maximum energy release rate criterion (Amestoy and Leblond, 1992). This means, that in the case of pure mode III, the crack propagates globally in a horizontal manner (Sommer, 1969). In bending experiments, as the front experiences mode II that changes sign from one side to the other, opposite tilt angles are observed, so that the front seems to progressively rotate until it aligns perpendicularly to the bending direction (Lazarus et al., 2008). On the microscopic scale, in contrast, the original crack tip undergoes fragmentation into facets due to the local mode III opening. These facets initiate at an angle to the mother crack and gradually coalesce during propagation, ultimately creating a jagged macroscopic surface. While the macroscopic problem is relatively straightforward to model (Gravouil et al., 2002; Citarella and Buchholz, 2008; Wu and Huang, 2020; Molnár et al., 2022), the phenomenon occurring at the micro-scale is much more complicated. Therefore, in this paper, we will specifically concentrate on the micro-scale initiation of the facets. Furthermore, we limit our focus to pure mode III loading, which poses distinct challenges, as discussed below.

Most analytical studies of crack front instability focus on mixed mode I+III loading, using linear stability analysis that considers the evolution of small perturbations (Leblond et al., 2011; Leblond and Lazarus, 2015; Leblond et al., 2019; Vasudevan et al., 2020; Lebihain et al., 2022). The analysis seeks a helicoidal solution that assumes a constant energy release rate and relies on the principle of local symmetry. However, this solution has two major limitations. Firstly, when only mode III loading is present, the allowed perturbation reduces to 0 because crack opening is not satisfied along the new crack front. Secondly, due to the lack of an internal length-scale, the solution is unable to produce a finite initiation distance between facets, resulting in an infinitesimally small pitch (initiation distance) for the helicoid. Additionally, the linear stability limit predicted by this solution as a function of Poisson's ratio and mode mixity does not correspond to the experimental observations as facets generally form below this threshold (Pham and Ravi-Chandar, 2014).

As previously noted, there are few simulations available that address the fundamental process of initiation, with only a handful of models incorporating a finite length-scale to depart from Griffith's singular description. In the literature, researchers have employed various techniques, such as the phase-field method (Pons and Karma, 2010), material-point erosion method (Pandolfi et al., 2013), and more recently, the extended finite element approach (Shi et al., 2022). While the latter two methods show promise, accurately quantifying crack propagation remains a challenge. As a result, we will primarily focus our discussion on the phase-field model.

The first phase-field study to focus on simulating facet initiation was conducted by Pons and Karma (2010). They introduced infinitesimal random perturbations to the crack front and observed a helical crack pattern. They then estimated the fastest

growing wavelength for small mode mixing ratios. However, they only considered mixed I+III mode loading, with a predominant mode I contribution, and did not account for tension/compression energy decomposition in their model, meaning their cracks would have opened under compression in pure mode III. In their study, Chen et al. (2015) utilized this model to compare their results with experimental data. Their findings demonstrated a noteworthy aspect: the stability of straight propagation is subcritical. This implies that facet formation exhibits highly nonlinear behavior and can be initiated below the linear stability threshold, aligning with experimental observations. They initiated the helical crack pattern using a helical perturbation on the crack front and evaluated its growth or decay under different deformation states. The paper also provides insights into the coarsening phenomenon and the evolution of the facet angle. However, the authors did not provide any information on the characteristic initiation wavelength as a function of material parameters or mode mixity due to the aforementioned limitations. Contrary to both logic and experimental observations (Knauss, 1970), both works fail to predict facet formation in pure mode III loading. Subsequently, Henry (2016) employed mixed mode stress boundary conditions to investigate the coalescence of initially irregular crack fronts. The presented results were only validated for small amounts of antiplane shear. Given the considerable popularity of the phase-field model proposed by Bourdin et al. (2000), Pham and Ravi-Chandar (2017) were the first to utilize it for analyzing the facet initiation problem. Their paper presented pure mode III results, but they were unable to initiate facets in a pristine material and had to use relatively significant defects to induce daughter cracks. This resulted in an impact on the spacing between facets due to the initial model conditions. The authors concluded that an energy barrier might have prevented facet creation in antiplane shear. Later in this paper, we will further elaborate about the differences between our and existing phase-field models, and more particularly the model of Pham and Ravi-Chandar (2017).

Parallel to numerical simulations, researchers have also utilized the coupled criterion to study mixed mode I+III fracture (Mittelman and Yosibash, 2015; Yosibash and Mittelman, 2016; Doitrand and Leguillon, 2018b; Campagnolo and Sapora, 2021). The coupled stress-energy criterion has been successfully employed to assess crack front segmentation under mode I+III loading. Previous studies (Yosibash and Mittelman, 2016; Doitrand and Leguillon, 2018b; Doitrand et al., 2023) have focused on determining the initiation remote loading corresponding to a given angle and shape of a facet. However, it has been observed that the initiation loading for facet nucleation is larger than what is required for straight crack propagation, which raises questions about the experimental occurrence of facet nucleation (Mittelman and Yosibash, 2015). Recently, researchers have taken into account mode-dependent fracture properties and T-stress, leading to the identification of configurations that are more likely to result in facet nucleation rather than straight crack propagation, which aligns better with experimental observations (Doitrand et al., 2023). Existing works have primarily examined the determination of facet initiation angles under mixed mode I+III loading, considering either a single facet in an infinite medium (Mittelman and Yosibash, 2015; Yosibash and Mittelman, 2016) or a periodic array of well-separated facets (Doitrand et al., 2023). These studies have overlooked the influence of facet spacing. While the coupled criterion was successfully applied to evaluate the tendency of facet formation, none of these studies provided a combined description of the facet spacing, and the effect of material properties in pure mode III opening. Additionally, most studies assumed that the facets were sufficiently far apart from each other to avoid interaction, without discussing this

assumption's validity. Although the coupled criterion mostly utilizes an idealized crack shape, and the stress field remains singular, it shows promise in improving our understanding of the phenomena observed in numerical experiments (Molnár et al., 2020a).

While both analytical studies (Leblond et al., 2011), numerical simulations (Pons and Karma, 2010), and experimental investigations (Pham and Ravi-Chandar, 2014) have posited the crucial requirement for a regularization length in comprehending mode III fracture; the feasibility of determining the initiation distance on a small scale using straightforward and readily measurable material parameters, and thus establishing a suitable internal length scale, remains ambiguous. Consequently, additional research is imperative to gain a comprehensive understanding of the interplay between material properties and the initiation distance of facets.

In this paper, we introduce a phase-field model that utilizes a small spatial perturbation in toughness to determine idealized facet spacing. We focus on pure antiplane shear, that has not been studied elsewhere. A thorough parametric study demonstrates that the statistical results are independent of the perturbation field and can be considered characteristic of the material. By narrowing our focus in this way, we hope to gain a deeper understanding of the mechanisms behind facet initiation and provide a foundation for further research in this area. We emphasize that the obtained spacing is an upper limit, which can be reduced by the presence of defects. In parallel, we propose a rudimentary analysis using the coupled criterion, wherein we explain why initiation happens at a higher loading state with facets and estimate a characteristic initiation distance. This analysis allows us to establish a correlation between the regularization length used in phase-field calculations and the material's tensile strength.

The paper is structured as follows. First, our strategy is laid out in Section 2, then Section 3 presents the results obtained with the phase-field method. After which Section 4 describes the development of the coupled criterion. In Section 5, we compare and contrast the results obtained with the two methods, highlighting their similarities and differences. Finally, in Section 6, we draw conclusions based on our findings.

2. Theoretical framework

This section aims to introduce the mechanical problem and delineate the objectives of the analysis. It highlights the two methods – the phase-field technique and the coupled criterion – employed to address the current challenge.

These two methods have been chosen due to the incorporation of a characteristic length scale, either as an input parameter or through the combination of material properties. Given their well-established nature, this section offers a succinct overview of their fundamental principles, define the necessary input variables, and outline potential outputs. The primary emphasis is on comparing how these two methods facilitate facet formation, providing a nuanced understanding of crack propagation under pure mode III loading conditions.

2.1. Problem statement

Consider a planar crack with a straight crack front residing within an infinite linear elastic medium characterized by a Young's modulus (E), Poisson's ratio (ν), and critical fracture energy (g_{mat}) (see Fig. 2a). Our objective is to address the propagation of this crack under the influence of an increasing mode III loading, denoted as K_{III}, applied uniformly along the crack front.

In our investigation, we focus on two potential scenarios: (i) continuous development of facets from the initial front, as depicted in Fig. 2b, and (ii) abrupt nucleation of facets at discrete points along the front, shown in Fig. 2c. To explore the first possibility, we will employ the phase-field method, while for the second possibility, the coupled criterion will be used. Special attention is directed towards comparing the outputs of the two methods, with a specific focus on the distance between facets as a function of the material's characteristic lengths.

2.2. Regularization length in phase-field

The fundamental concept underlying phase-field models is to approximate the crack discontinuity using a smeared damage field (d). Typically, a single length scale parameter (l_c) is introduced to govern the extent of damage penetration within the material. The phase-field model balances the elastic and diffused fracture energies to determine the energetically favorable crack front. Various versions of the model exist, sharing common inputs: the elastic constants E, and ν; the fracture toughness g_{mat}; and the regularization length l_c. Detailed information about the phase-field model used herein will be provided in Section 3.

Utilizing the Π-Vaschy-Buckingham theorem (Vaschy, 1892; Buckingham, 1914), we can construct dimensionless variables using two independent physical units. By selecting l_c and E, we normalize the critical loading $\frac{K_{\text{III}}^{cr}}{E\sqrt{l_c}}$ and the facet spacing $\frac{\Lambda}{l_c}$ and express these quantities as a functions of the normalized critical energy release rate $\frac{g_{\text{mat}}}{El_c}$ and Poisson's ratio ν. Introducing the normalized critical loading for straight crack initiation (Irwin, 1957):

$$\frac{k_{\text{IIIc}}}{E\sqrt{l_c}} = \frac{\sqrt{\frac{g_{\text{mat}}E}{1+\nu}}}{E\sqrt{l_c}} \tag{1}$$

we can equivalently express $K_{\text{III}}^{cr}/k_{\text{IIIc}}$ and $\frac{\Lambda}{l_c}$ as a functions of $\frac{g_{\text{mat}}}{El_c}$ and ν.

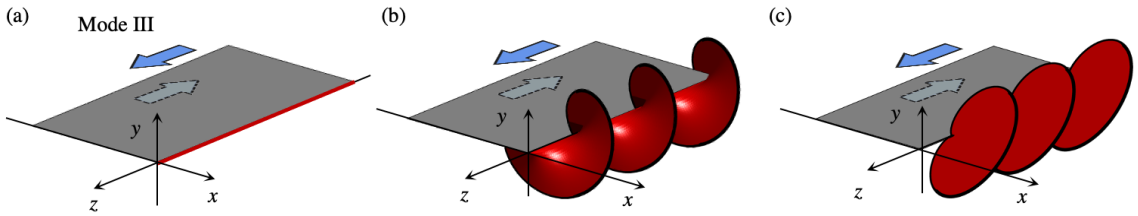

Figure 2: Mode III crack front segmentation: (a) Problem definition; (b) continuous formation; (c) abrupt facet emergence. The mother crack is displayed in gray, while the facets are shown in red. The blue arrows show the direction of the macroscopic shear applied in the yz plane.

2.3. Irwin's length and the coupled criterion

The fundamental concepts of the coupled criterion combines the incremental form of Griffith's energy release rate with a stress threshold criterion. The method assumes a predetermined shape and array of cracks at nucleation. The extent of the crack surface is identified where both the incremental energy release rate exceeds the fracture toughness, and the nominal opening stress surpasses the material's tensile strength over the entire newly opened crack surface. Similarly to the phase-field model, the elastic medium in the coupled criterion is characterized by Young's modulus E and Poisson's ratio ν, with the materials fracture toughness g_{mat}. However, instead of regularizing the crack, a tensile strength σ_c is introduced. Further details of the method used herein is given in Section 4.

The introduction of a stress criterion reveals the emergence of a characteristic length, such as an arrest length or characteristic crack spacing (Faria Ricardo et al., 2020). For dimensional reasons, this length is linked to Irwin's length (Leguillon and Yosibash, 2003; Martin et al., 2018), which relates Young's modulus, fracture toughness, and tensile strength by the following formula:

$$l_{\text{mat}} = \frac{E g_{\text{mat}}}{\sigma_c^2}. \tag{2}$$

As before, for dimensional reasons, the coupled criterion yields the normalized critical loading ($K_{\text{III}}^{cr}/k_{\text{IIIc}}$), and the normalized facet spacing (Λ/l_{mat}) as a function of the normalized fracture toughness $g_{\text{mat}}/(El_{\text{mat}})$ and ν.

2.4. Equivalence between the two lengths

The phase-field method and the coupled criterion offer distinct approaches for modeling cracks. The phase-field method allows the crack to evolve continuously, enabling us to capture the formation of complex crack patterns. On the other hand, the coupled criterion adopts a discrete fracture approach, representing cracks as discrete, predetermined entities and focusing on single critical loading for crack initiation.

As observed earlier, both methods are capable of determining the initiation spacing Λ, but they rely on distinct characteristic lengths. The phase-field method yields Λ/l_c as a function of ν and $g_{\text{mat}}/(El_c)$, whereas the coupled criterion provides Λ/l_{mat} as a function of ν and $g_{\text{mat}}/(El_{\text{mat}})$. While l_{mat} can be derived from mechanical parameters, the physical meaning and measurement of l_c remains an open question, particularly in the context of mode III loading.

In this paper, our goal is to establish a connection between the initiation distance among echelon cracks and quantifiable material parameters. This is accomplished by employing a combination of the phase-field method (elaborated in Section 3) and the coupled criterion (explored in Section 4). We assess these outcomes in comparison to l_c and l_{mat} in Section 5.

3. Phase-field study

This section offers insight into the simulation details and showcases the outcomes of employing the phase-field approach to simulate crack initiation and propagation under pure mode III conditions. Section 3.1 outlines the model and the post-processing method employed to examine facet formation. The impact of model parameters is discussed in Section 3.2, followed

by the presentation of material parameter effects in Section 3.3. Briefly, in Section 3.4, the results of present model is compared to the ones obtained in the literature. Lastly, Section 3.5 provides a summary of the findings from the phase-field study.

3.1. Phase-field model

3.1.1. Phase-field theory

Bourdin et al. (2000) introduced the currently widely used theory for modeling fracture using variational methods. It is fundamentally based on the idea of damage mechanics (Kachanov, 1958) and the regularization of a discontinuity with a continuous field (Ginzburg and Landau, 1950; Cahn and Hilliard, 1958). The new theory replaced the discrete fracture surface, as originally formulated by Griffith (1921, 1924), within the variational framework proposed by Francfort and Marigo (1998). Instead of a discrete crack surface, a continuous damage density function was employed. This transformation of the original minimization problem involved the utilization of the Mumford and Shah functional (Mumford and Shah, 1989), which is a specific case within the broader Ambrosio and Tortorelli elliptic regularization framework (Ambrosio and Tortorelli, 1990). The phase-field fracture model was founded on the diffuse representation of localized discontinuities, where the crack surface is approximated using a damage variable (d) that ranges from 0 to 1. When the phase-field is 0, the domain is undamaged, while a value of 1 indicates that the crack has fully formed, and the material has lost all of its resistance and stiffness. This approach allows for the gradual transition from an intact material to a fully fractured state, thus enabling the simulation of crack initiation and propagation without the need for explicit crack tracking. The evolution of damage in phase-field models is dictated by a system of partial differential equations. This phase-field problem is commonly coupled with equations that describe the mechanics of the material; in this context, linear elasticity. As damage evolves, it influences the mechanical behavior of the material, instigating the initiation and propagation of cracks. Fundamentally, the energy of the solid body, as shown in eq. (3), is minimized. In this process, the accumulation of elastic energy drives the formation of damage and the subsequent opening of cracks.

There are several phase-field models available in the literature (Bourdin et al., 2000; Miehe et al., 2010a; Ambati et al., 2015; Wu, 2018b). In this paper, we employed the AT1 model proposed by Pham et al. (2011), which incorporates a classic quadratic energy degradation function with a linear crack surface density equation. This model is preferred due to its ability to provide an initial elastic threshold, which is essential for accurately simulating the onset of damage. The AT1 model has been extensively validated and widely used in fracture simulations in various materials science applications (Ambati et al., 2015; Tanné et al., 2018). To enforce positive damage increments and irreversibility, we adopted Lagrange multipliers (Lu et al., 2020) in our implementation. For a deeper comprehension of the phase-field theory, we recommend interested readers consult the works of Bourdin et al. (2000) and Miehe et al. (2010a). As for implementation details, we direct readers to our recent publication (Molnár et al., 2022), where additional information is provided. For sake of self-consistency, we highlight the main ingredients that are relevant to this particular study.

The internal energy of the solid is described with the following equation:

$$\begin{aligned}\Pi(\mathbf{u},d) &= E(\mathbf{u},d) + W(d) \\ &= \int_{\Omega} \left[g(d)\,\psi_0^{+}(\mathbf{u}) + \psi_0^{-}(\mathbf{u}) \right] d\Omega \\ &+ \int_{\Omega} \left[\frac{3g_c}{8l_c} \left(d + l_c^2 |\nabla d|^2 \right) \right] d\Omega.\end{aligned} \tag{3}$$

The strain and fracture energy components are denoted as E and W, respectively and $\mathbf{u}$ is the sought displacement field on a domain Ω. Fracture energy can be described using two parameters: the numerical critical energy release rate, g_c, and the crack density function. The diffusion of damage is controlled by the length scale l_c. The undamaged strain energy density, ψ_0, is separated into positive (ψ_0^+) and negative components (ψ_0^-). Only the positive (tensile) component is subject to damage, which is represented using a quadratic degradation function: $g(d) = (1-d)^2$. This means that only tensile energies contribute to the formation of cracks. To distinguish between tensile and compressive strain energies, the decomposition proposed by Bernard et al. (2012) was adapted:

$$\psi_0^{+,-} = \sum_{i=1}^{3} \mu \langle \varepsilon_i \rangle_{+,-}^2 + \frac{\lambda}{2} \langle tr(\varepsilon) \rangle_{+,-}^2 . \tag{4}$$

The eigenvalues, denoted as ϵ_i, are computed using the infinitesimal strain tensor, defined as $\varepsilon = \nabla^S u$. The material parameters λ and μ are Lamé parameters. Functions $\langle \rangle_{\pm}$ stand for: positive $\langle x \rangle_+ = (x + |x|)/2$ and negative $\langle x \rangle_- = (x - |x|)/2$ parts.

The fracture surface in the phase-field technique was obtained by integrating the crack surface density function over the entire domain:

$$S = \int_{\Omega} \frac{3}{8l_c} \left[d + l_c^2 |\nabla d|^2 \right] d\Omega. \tag{5}$$

In Fig. 3a, we present the geometric configuration of the phase-field model employed in our study. We commence with an initial planar mother crack, characterized by a straight front, within a cylinder of radius R and length L. The intention was to use sufficiently large values of R and L to emulate behavior in a medium with properties approaching that of infinity (as depicted in Fig. 2a). Consequently, we applied elastic K-field displacement boundary conditions, representative of pure mode III, to the cylinder's mantle:

$$\hat{u}_x = 0, \hat{u}_y = 0, \hat{u}_z(r,\theta) = \frac{K_{\mathrm{III}}}{\mu} \sqrt{\frac{2r}{\pi}} \sin\frac{\theta}{2}, \tag{6}$$

where K_{III} is a loading parameter, which represents the apparent mode III stress intensity factor at initiation. Parameter μ is the shear modulus, r and θ are the polar coordinates in the xy plane. We imposed periodic boundary conditions in the z

direction for all degrees of freedom located on the lateral faces of the cylinder. The initial mother crack was included both in the geometry (node splitting) and with a $\hat{d} = 1$ Dirichlet boundary condition. Note that in the undamaged state, the displacement field conforms to eq. (6) across the entire domain within the precision of the finite element approximation.

The mechanical and damage phase-field problems were solved in a staggered, weakly coupled fashion. The load step was automatically controlled using the elastic energy increment scheme proposed by Molnár et al. (2020b,a). A parametric study, presented in details in Appendix A, investigates the influence of the load step size on the convergence of crack patterns. The simulation employs a mesh consisting of fully integrated, eight-node, linear hexahedral elements, with an average size of $h_{\mathrm{PF}} = l_c$. It is worth mentioning that, even though the critical loading is influenced by the coarse mesh (Miehe et al., 2010a; Tanné et al., 2018; Molnár et al., 2022), we have observed no impact of the ratio l_c/h_{PF} on the crack pattern, as demonstrated in Fig. A.24 in Appendix A.

The material's response was evaluated at Gaussian integration points, while the phase-field is determined at the nodes, introducing a localization error. Hence, in our comparison with the coupled criterion, we mitigate the localization error as described by Molnár et al. (2022) by introducing a numerical fracture toughness. To fully open a crack, it is crucial for the damage to uniformly approach 1 across the entire element. This, in conjunction with the crack's presence, results in an apparent increase in the model's effective toughness. To counteract this effect, the numerical toughness (g_c) was adjusted using the following equation (Bourdin et al., 2008; Linse et al., 2017; Tanné et al., 2018):

$$g_c = g_{\mathrm{mat}} \left(1 + \frac{3h_{\mathrm{PF}}}{8l_c}\right)^{-1}, \tag{7}$$

where h_{PF} represents the characteristic mesh size of the model and g_{mat} is the materials fracture toughness. When the ratio l_c/h_{PF} is significantly large, the procedure of distinguishing between g_c and g_{mat} can be omitted, as g_c approaches g_{mat}. This ensures consistency in the comparison and has been widely adopted in the literature.

3.1.2. Inhomogeneous fracture toughness

As highlighted by Pham and Ravi-Chandar (2017), initiating facets in anti-plane shear does not occur if no perturbation is applied in the model. To solve this issue, we propose in this paper to introduce a 3D Gaussian random field[1] (GRF) (Lang and Potthoff, 2011; Dietrich and Newsam, 1997) to spatially alter the critical fracture toughness (g_c) of the material.

The covariance function used to define the GRF in this study is given by:

$$cov\left(\Delta x, \Delta y, \Delta z\right) = \sigma_G^2 \exp\left[-\left(\frac{\Delta x}{l_G}\right)^2 - \left(\frac{\Delta y}{l_G}\right)^2 - \left(\frac{\Delta z}{l_G}\right)^2\right]. \tag{8}$$

[1]Gaussian random fields are stochastic processes that are defined by a set of random variables that follow a Gaussian distribution. These random variables are defined over a continuous spatial domain and are correlated with each other according to a specified covariance function. Gaussian random fields are commonly used in numerical simulations as a tool for generating spatially correlated random fluctuations in a given parameter, such as the toughness of a material, which can be used to initiate defects or irregularities in the simulation.

The covariance function used to define the GRF is a measure of the correlation between different points in the field. Specifically, it describes how the variation in one point is related to the variation in another point, as a function of their distance. The covariance function (8) used in this study has a Gaussian form and depends on the distance (Δx, Δy, Δz) between two points in the field, and a length scale parameter, l_G, which controls the decay of the correlation with distance. The standard deviation of the GRF, σ_G, determines the overall magnitude of the perturbation to the material's toughness. The GRF was periodic only in the z direction. The histogram and a 2D slice of the generated random field is depicted in Fig. 3b and 3c respectively.

3.1.3. Elementary crack shape

In this subsection, we initially illustrate how the model operates and generates facets in antiplane shear. Subsequent sections delve into the impact of material properties on its key features. The material was considered linear elastic with a Poisson's ratio of $\nu = 0.37$ and with a normalized fracture toughness of $g_c/(El_c) = 1$. The parameters of the GRF were set to $l_G = l_c$ and $\sigma_G = 10^{-3} g_c$. The influence of the GRF and the material parameters are discussed in Sections 3.2.1 and 3.3. The results in this section were obtained for $R = 20l_c$ and $L = 80l_c$. Extensive verification confirms that these dimensions were sufficiently large to ensure that the boundaries do not influence the form or behavior of the crack at initiation (see Fig. A.23 in Appendix A).

Fig. 4 displays the isosurface[2] of the damage for $d = 0.8$ at the beginning of the propagation. The lower part of the figure shows the 3D view of the fully initiated daughter cracks before coarsening, while the upper part displays the crack in the xz, xy, and yz planes. As the isosurface highlights only the region where $d = 0.8$, the damaged zone around the mother crack tip appears blank, therefore to highlight this area where $d > 0.8$, we have enclosed it with a blue circle.

Initially, a homogeneous damage zone emerged around the tip of the mother crack, exhibiting self-similarity in the z direction.

[2] An isosurface is a three-dimensional surface that represents a constant value of a scalar field. In other words, it is a surface that connects points in space where a particular scalar field has the same value.

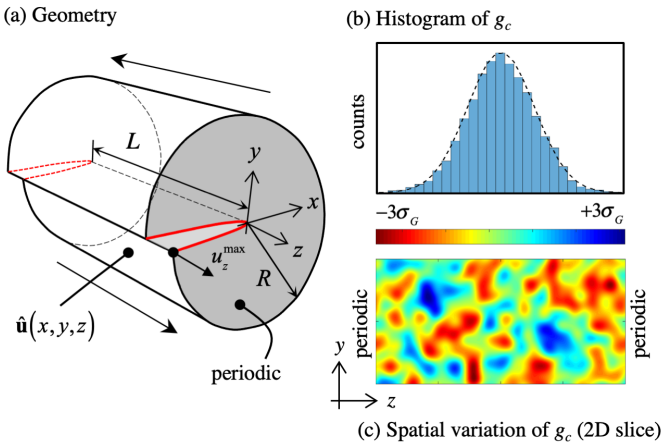

Figure 3: (a) The geometry and boundary conditions of the phase-field model are depicted. (b) The histogram shows the variation applied by the Gaussian random field (GRF) used to induce facets in the model. (c) A 2D example of the GRF is also shown. Both the abscissa of the histogram and the color bar are scaled between -3σ_G and +3σ_G.

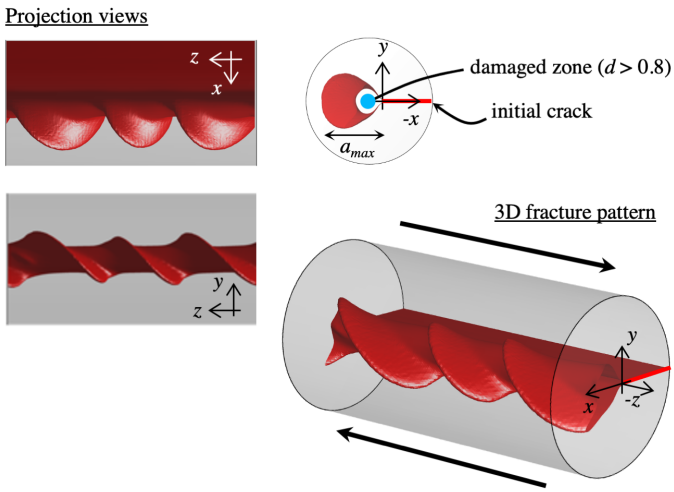

Figure 4: Typical crack pattern obtained from the phase-field model under antiplane shear. The red surface in the figure corresponds to the isosurface[3] of the damage variable at $d = 0.8$, with a model size of $R = 20l_c$ and $L = 80l_c$ and material parameters $g_c/(El_c) = 1$ and $\nu = 0.37$.

By increasing the load, upon the onset of localization, daughter cracks began to form within a characteristic distance. The fully developed daughter cracks took on a fin-like shape, extending in the positive x direction. The upper and lower portions of the cracks curved back and reconnected with the mother front, creating a recurring pattern reminiscent of the form proposed by Leblond et al. (2011). There was an additional advancement of the helicoid spiral in the x direction compared to the aforementioned analytic solution.

As supplementary material (Appendix B), we have included two components. Firstly, a movie showcasing the behavior of the large $R = 40l_c$ and $L = 200l_c$ model with $\nu = 0$, providing a comprehensive visual representation. Secondly, we have included a small example input file that can be executed on a desktop computer. This example features $\nu = 0$, $L = 15l_c$, and $R = 20l_c$, allowing for a practical and manageable demonstration.

3.1.4. Quantitative description

To provide a more refined description of the crack pattern, we propose to use two key metrics: the average distance between neighboring facets at initiation and the maximum tilt of the daughter cracks. However, defining an accurate initiation distance poses a challenge due to the inherent coarsening that takes place in the phase-field approach. Therefore, we plotted the average distance between facets as a function of their extent in the x direction. This was achieved by capturing slices of the isosurface (with $d = 0.8$) aligned with the yz plane at $x = a$, and then measuring the distance between the centers of individual contours within these slices. The visualization and methodology are illustrated in Fig. 5. This approach yields the average distance between facets at a given distance a.

The angle of the facet was determined by identifying the contour edge of the facet, as illustrated at the bottom part of Fig. 5 using black solid lines. Subsequently, the angle of this contour was measured with respect to the z axis within the yz plane at

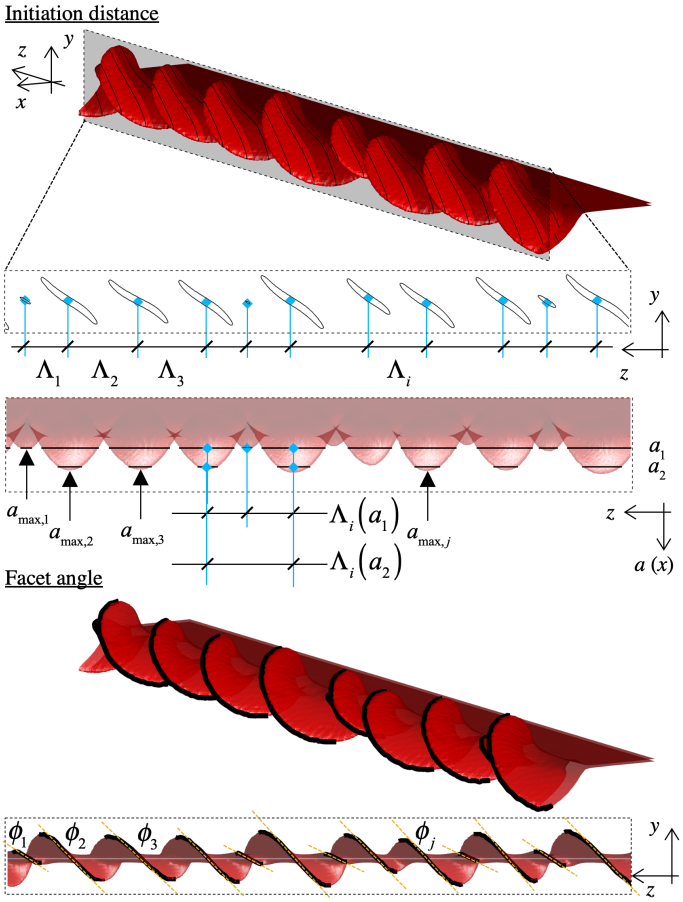

Figure 5: Schematic illustration of the method used to measure the initiation distance between neighboring facets and the facet angle (with a model size of $R = 20l_c$ and $L = 200l_c$ and material parameters $g_c/(El_c) = 1$ and $\nu = 0.37$).

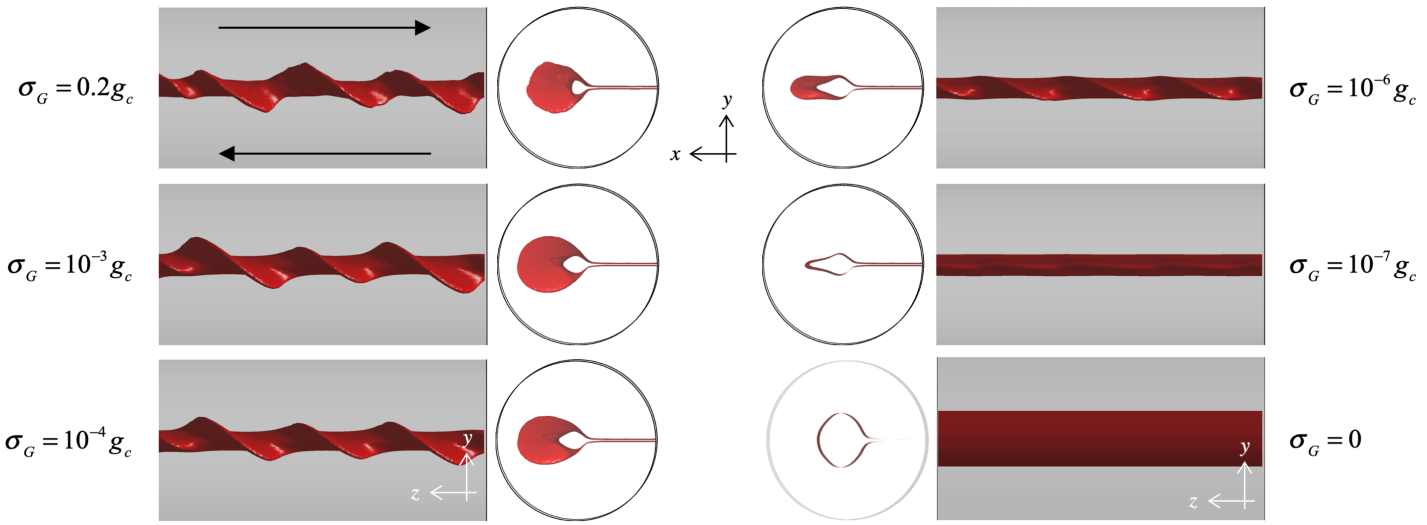

Figure 6: Effect of GRF variation (σ_G) on the crack pattern for the same loading with $l_G = lc$. The simulation domain dimensions were $L = 80l_c$ and $R = 20l_c$ with material parameters $g_c/(El_c) = 1$ and $\nu = 0.37$.

the facet's maximum extent, indicated as $x = a_{\max}$.

3.2. Effect of model parameters

The paper aims to establish a correlation between material parameters and the properties of emerging cracks. Consequently, it is imperative to identify how model parameters influence the formation of crack patterns. Therefore, in the following sections, the effect of the perturbation field and then the effect of the energy decomposition scheme is analyzed.

3.2.1. Toughness perturbation

We have demonstrated that perturbing spatially the toughness proved to be a viable strategy to inducing facets. The perturbation could be considered physically meaningful as it represents a variation in the material's structure. However, to explore facet initiation in a quasi-perfect material, we strove to find a set of Gaussian random field parameters that do not statistically influence the initiation of facets. Therefore, a series of tests were carried out to investigate the impact of the GRF parameters on the crack pattern. In this section the material parameters were kept fixed at $\nu = 0.37$ and $g_c/(El_c) = 1$.

Fig. 6 illustrates the effect of the magnitude of the variation in toughness (σ_G) on the crack pattern with $l_G = l_c$ and a fixed random seed. The results reveal that σ_G has a pronounced effect on the crack shape while having little impact on the initiation distance between neighboring facets. Initial signs of localization became detectable at $\sigma_G = 10^{-7}g_c$, and this localization became distinctly visible after reaching $\sigma_G = 10^{-6}g_c$. As the modification progresses, it began to influence the shape of the crack, leading to a less defined damaged zone above $0.2g_c$, as illustrated in the upper left figure. Within the range of $[10^{-7} - 10^{-1}]g_c$, no discernible alterations were observed in the position or distance between the initial localizations. Additional results for $\sigma_G = [10^{-1}, 10^{-2}, 10^{-5}, 10^{-8}]g_c$ are presented in Appendix A. For further analysis, we choose the smallest perturbation, which

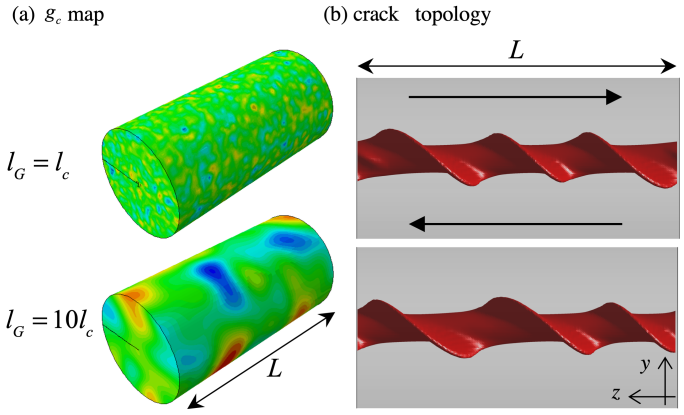

Figure 7: Effect of GRF length scale on the crack pattern with the same random seed. (a) g_c map corresponding to $\sigma_G = 10^{-3}g_c$. The colors in the figure represent a variation of approximately -3σ_G to +3σ_G. The GRF is displayed with $l_G = l_c$ on the top and $l_G = 10l_c$ on the bottom. (b) Corresponding phase-field crack patterns with $g_c/(El_c) = 1$ and $\nu = 0.37$. The simulation domain dimensions were $L = 80l_c$ and $R = 20l_c$.

gave the most pronounced facets, thus $\sigma_G = 10^{-3}g_c$. This value can be considered small enough to ensure that the results are statistically independent of the GRF.

Fig. 7 shows the effect of the GRF length scale (l_G) on the crack pattern obtained for the same random seed and $\sigma_G = 10^{-3}g_c$. Tests with $l_G < l_c$ were not included due to the homogenizing effect of the phase-field method, which would make it difficult to observe any significant differences in the resulting crack pattern. The results in Fig. 7 demonstrate that the crack patterns obtained for different GRF length scales with the same random seed and a small σ_G are similar, with only a slight shift to the right. Furthermore, the initiation distance between facets remains unchanged and is not affected by the ratio l_G/l_c. In addition, in Fig. A.22 in Appendix A presents the results obtained using two additional random seeds. The results show that while the GRF did affect the exact position of the facets, it had little impact on their spacing.

In summary, these results indicated that the crack pattern is primarily influenced by loading and material parameters, rather than the specific realization of the Gaussian random field (GRF) with reasonably small fluctuations. While the local toughness variation induced by the GRF can be viewed as inherent fluctuations in the material's structure, our primary objective in this paper was to identify a sufficiently small perturbation that does not significantly impact initiation statistically. Consequently, by analyzing a quasi-pristine material sample, we can establish a link between material properties and the crack pattern. For subsequent simulations, we fixed $l_G = l_c$ and $\sigma_G = 10^{-3}g_c$ for a reference GRF.

3.2.2. Energy decomposition scheme

We also investigated the impact of the energy decomposition scheme on the crack pattern, using an identical GRF field. Fig. 8 showcases the crack patterns obtained with different energy decomposition methods. Part (a) presents the crack pattern with the spectral energy decomposition scheme (see eq. 4) used in previous studies. In this case, both the hydrostatic and deviatoric components of the tensile strain energy were distinguished. Notably, the facets were present, and they exhibited localization at equal distances.

In contrast, part (c) illustrates the crack's form when no decomposition was utilized and the energies were defined as $\psi_0^+ = \sum_{i=1}^{3} \mu\varepsilon_i^2 + \frac{\lambda}{2} tr(\varepsilon)^2$ and $\psi_0^- = 0$. As a result, both tensile and compressive components of the strain tensor induced damage, leading to a horizontal crack without any facets.

Finally, part (b) demonstrates the situation where only the hydrostatic component was separated as: $\psi_0^+ = \sum_{i=1}^{3} \mu\varepsilon_i^2 + \frac{\lambda}{2} \langle tr(\varepsilon) \rangle_+^2$ and $\psi_0^- = \frac{\lambda}{2} \langle tr(\varepsilon) \rangle_-^2$. In this case, the crack also propagated horizontally with no facets present.

These observations show that omitting the split on the deviatoric component resulted in a horizontal propagation without facet formation. This phenomenon underscores the importance of not only distinguishing between hydrostatic tension and compression alone, as it is insufficient for accurately modeling facet formations in antiplane shear. Instead, the inclusion of local tensile opening at the crack tip is critical to get facets to form.

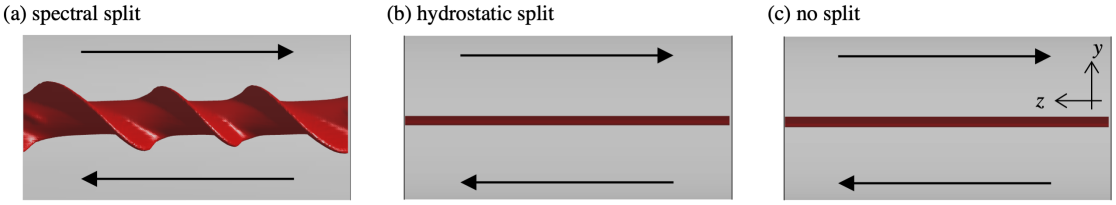

Figure 8: Effect of different energy decomposition schemes on the crack pattern (with a model size of $R = 20l_c$ and $L = 80l_c$ and material parameters $g_c/(El_c) = 1$ and $\nu = 0.37$).

3.3. Effect of material parameters

In this section, our objective is to investigate the impact of material parameters, specifically $g_c/(El_c)$ and ν on the forming crack facets. The GRF parameters were held constant at $l_G = l_c$ and $\sigma_G = 10^{-3} g_c$. To ensure statistical significance in our results, we extended the length of the model to $L = 200l_c$. Two model diameters were considered: $R = 20l_c$ and $40l_c$, to which we will refer to as the small and the large model in the following.

Due to computational constraints, we analyzed two large simulations, each comprising 6.3 million degrees of freedom. These computations took 6-8 weeks on a 24-core cluster node. The analysis encompassed two limit cases, namely $\nu = 0$ and $\nu = 0.45$, with a fixed value of $g_c/(El_c) = 1$. In order to explore the transition between these aforementioned limits, we utilized smaller models, completing them within 6 days. For the small model we varied the material properties within the ranges of $\nu = [0 - 0.37]$ and $g_c/(El_c) = [0.1 - 10]$.

Consistent with the approach in previous sections, we initially present the overall behavior in Section 3.3.1. Subsequently, we delve into specific details, discussing the average distance between neighboring facets at initiation in Section 3.3.2, the evolution of the facet tilt in Section 3.3.3, and the critical loading at initiation in Section 3.3.4.

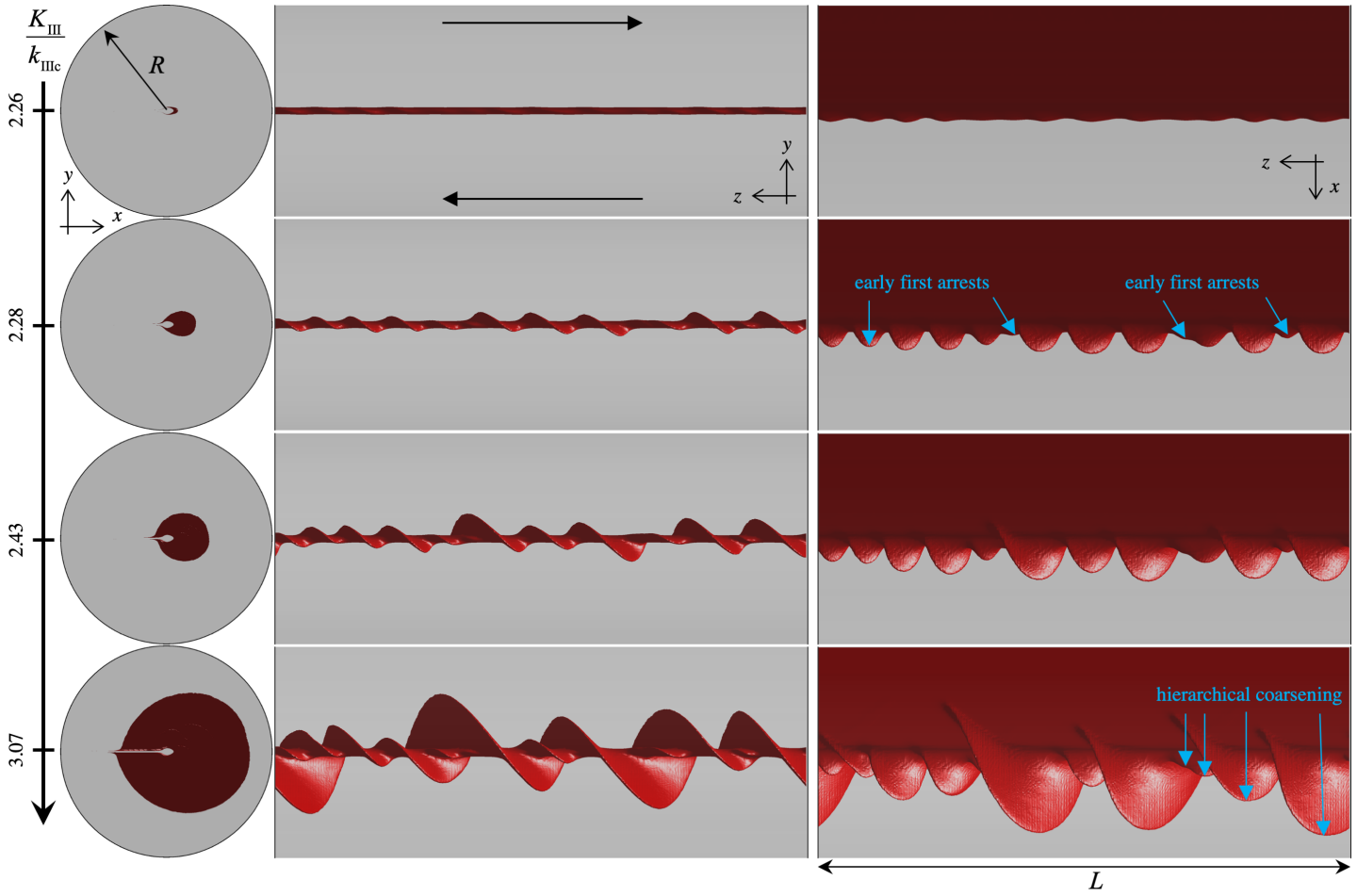

Figure 9: Crack evolution for increasing K_{III}/k_{IIIc} in the large model with $\nu = 0$, $R = 40l_c$ and $L = 200l_c$ (with $g_c/(El_c) = 1$).

3.3.1. Screening effect and coarsening

The evolving crack pattern for various normalized loading stages is depicted in Fig 9 for the large model with $\nu = 0$. The load parameter (K_{III}) was normalized with the critical value defined in eq. (1) for horizontal initiation.

Fig. 9 shows, that at initiation ($K_{III}/k_{IIIc} = 2.26$) the straight crack front underwent a transition where slight ruffling occurred and small undulated forms became apparent. In the subsequent stage, these undulations began to grow, gradually forming incipient facets. At this point, the facets exhibited a relatively shallow angle, approximately 30°. In the third row, corresponding to $K_{III}/k_{IIIc} = 2.42$, it became evident that certain daughter cracks halted their propagation. The screening effects prompted adjacent nodes to expand and to fill the void left by the arrested cracks. In the subsequent row, a distinct observation emerges as various facets arrested at diverse lengths. This progression gave rise to a crack pattern characterized by a hierarchical structure, showcasing a discernible coarsening phenomenon.

In the scenario characterized by a Poisson's ratio of $\nu = 0.45$ (Fig. 10), the initial undulations exhibit a reduction in magnitude, and only larger fragments commence and expand. Owing to the initiation occurring at a comparatively greater distance, the fragments grow in a more uniform fashion, leading to a greater degree of equidistant length.

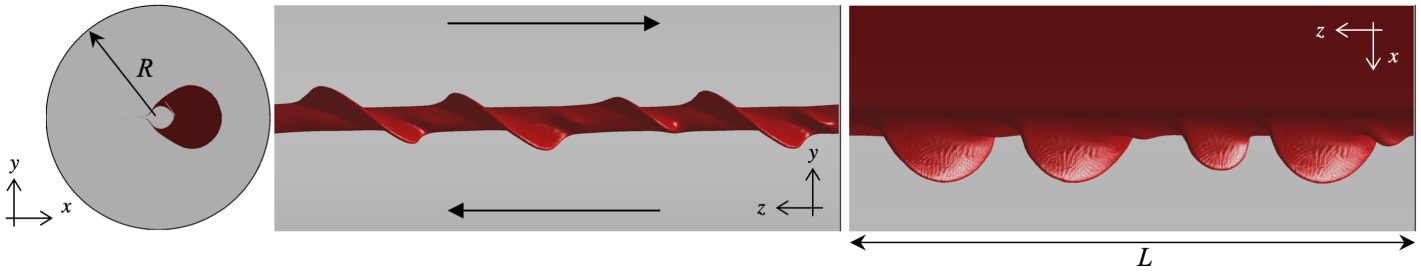

Figure 10: Crack pattern for $\nu = 0.45$ and $K_{\mathrm{III}}/k_{\mathrm{IIIc}} = 3.92$ in the large model with $R = 40l_c$ and $L = 200l_c$ (with $g_c/(El_c) = 1$).

3.3.2. Average facet distance

We recall that for dimensional reasons, the normalized facet spacing at initiation (Λ/l_c) supposed to depend only on $g_{\mathrm{mat}}/(El_c)$ and ν. We took precautions to ensure the use of a sufficiently large domain and a small enough perturbation to obtain accurate results. In Fig. 11a, the influence of the critical energy release rate (fracture toughness) is illustrated. It is observed that a hundred-fold magnification of $g_c/(El_c)$ has no discernible impact on the evolution of crack patterns, particularly during the initiation phase under normalized loading. Both $K^{cr}_{\mathrm{III}}/k_{\mathrm{IIIc}}$ and Λ/l_c are independent of $g_c/(El_c)$, and consequently, from $g_{\mathrm{mat}}/(El_c)$ based on the relationship between g_{mat} and the numerical toughness g_c, as shown in eq. (7).

Furthermore, Fig. 11b demonstrates the impact of varying Poisson's ratio in the small model. Similarly to the results shown in Fig. 9 and 10 for the large model, our observations indicate that increasing Poisson's ratio leads to a larger process zone, evidenced by the presence of more homogeneous damage surrounding the mother crack tip. We also noted that small cracks, which quickly arrested in low ν scenarios, did not appear for larger Poisson's ratios.

To investigate the quantitative impact of Poisson's ratio on the initiation distance between neighboring facets, we have calculated Λ in various cuts. The results are summarized in Fig. 12a. It is shown, that for smaller values of Poisson's ratio, smaller cracks can initiate and propagate, while for larger values of ν, smaller cracks arrest at a shorter distance. The average facet distance and its standard deviation are displayed in Fig. 12b at $a = 4l_c$. However, smaller advancement values cannot be

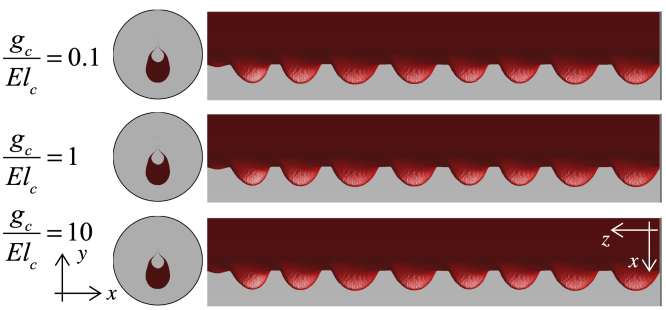

(a) Effect of fracture toughness on the crack pattern with the normalized loading of $K_{\mathrm{III}}/k_{\mathrm{IIIc}} = 3.56$.

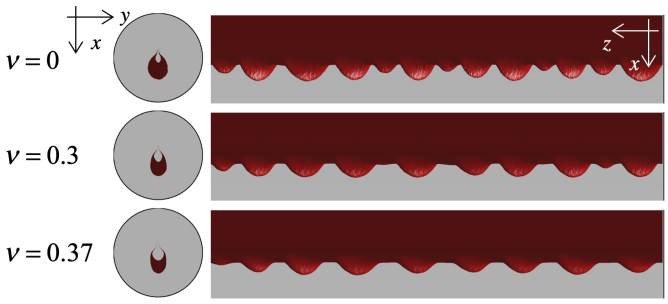

(b) Effect of Poisson's ratio on the crack pattern at initiation with the same maximum crack extension ($\max(a_{\max,i}) = 10l_c$). The normalized loading was taken respectively $K_{\mathrm{III}}/k_{\mathrm{IIIc}} = 2.56$, 2.87 and 3.27 for $\nu = 0$, 0.3 and 0.37.

Figure 11: Effect of material properties on the crack pattern at initiation with $R = 20l_c$ and $L = 200l_c$.

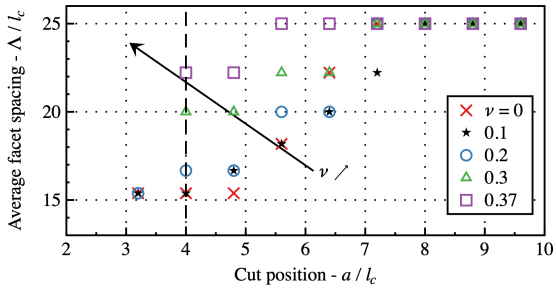

(a) Average normalized localization distance as a function of the position of the cutting plane for different ν.

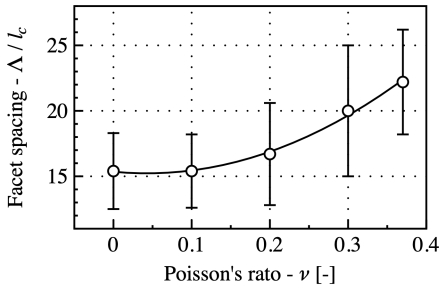

(b) Normalized average distance between neighboring facets at initiation and its standard deviation (on one simulation) as a function of Poisson's ratio (ν) in the phase-field simulation at a distance $a_{\max} = 4l_c$. The results are fitted using the quadratic function (9).

Figure 12: Effect of Poisson's ratio on the normalized average facet distance for the smaller model with $R = 20l_c$ and $L = 200l_c$.

determined from the figures due to the initial homogeneous damage field.

The results presented in Fig. 12b were fitted using a second-order polynomial. The coefficient of determination[3], R^2=0.99, indicates a high degree of correlation between the fitted curve and the data points. The polynomial equation used for the fitting is as follows:

$$\frac{\Lambda}{l_c} = 15.4 - 5.7\nu + 66.7\nu^2 \equiv \tilde{\Lambda}_{\mathrm{PF}}(\nu)\,. \tag{9}$$

It is important to note that these values are subject to change based on the selected threshold and the loading state of crack measurements. Nevertheless, they provide a valuable estimation of how facets interact in relation to Poisson's coefficient.

Due to coarsening these distances are subject to change. Therefore, we have displayed the normalized average facet distance

[3]The coefficient of determination is defined by $1 - \frac{SSE}{SST}$, where SSE is the sum of squared error and SST is the sum of squared total deviation from the mean in a least squares regression model.

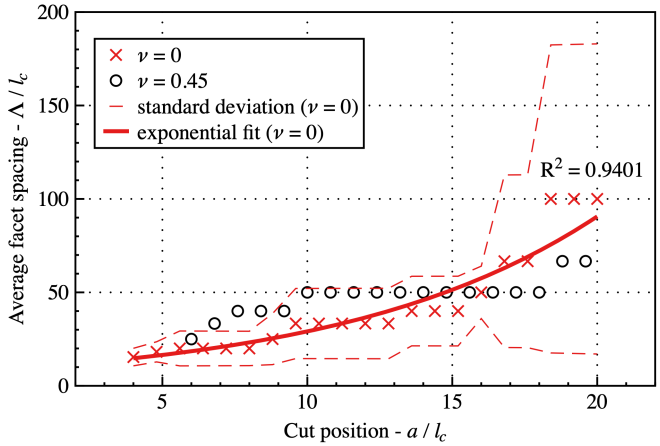

Figure 13: Evolution of normalized facet distance as a function of the position of the cutting plane for a fixed loading. The dashed lines represent the standard deviation. The measured values are fitted with the exponential function: $\Lambda/l_c = \alpha e^{\beta \frac{a}{l_c}}$. The model dimensions were $R = 40l_c$ and $L = 200l_c$.

and its standard deviation in Fig. 13 for the large model, where the facets were able to evolve. The loading was fixed at $K_{\mathrm{III}}/k_{\mathrm{IIIc}} = 3.07$ for $\nu = 0$, and 3.92 for $\nu = 0.45$ respectively. Then the position of the cutting plane was varied.

As the cutting plane advances, the average facet distance increases for both samples, indicating coarsening of daughter cracks. The discrete jumps in the function is due to the limitations in size of our model. When we lose a crack, the average distance jumps. In other words, as we start with approximately a dozen cracks, losing one on a finite length results in a visible finite jump. Nevertheless, an approximate initiation distance between facets can be measured, and the tendencies can be made clear. The evolution of the facet coarsening is fitted with an exponential curve, which qualitatively corresponds well to experiments conducted on inclined notched, bent samples (Hattali et al., 2021).

The distinguishing factor between the two cases lies in the behavior during propagation. For $\nu = 0.45$, all four daughter cracks propagate in unison within the range of $a/l_c = 10 - 18$, exhibiting a smaller standard deviation compared to the $\nu = 0$ case (which is not depicted in the figure). Conversely, in the case of $\nu = 0$, the coarsening phenomenon is notably more dramatic and takes precedence over the scenario with the higher Poisson's coefficient, manifesting after $a/l_c = 15$.

3.3.3. Facet angle

When analyzing the distance between facets, we can select an advanced loading stage and segment it into different slices. In contrast, facet angles undergo variations during propagation and coarsening, and therefore, their assessment occurs at different loading stages.

Facets initially appear at lower angles (approximately 25°) and gradually steepen. The impact of Poisson's coefficient shown in Fig. 14a is small. The average facet angle at the same $a_{\max}$ tends to be slightly smaller with an increase in ν. However, due to spatial limitations in the small model, it is challenging to conclude whether this effect is transitory or if it also influences $\phi_{\max}$ on the plateau.

In the large model, we observed the gradual increase in the tilt angle from quasi-horizontal as the crack advances. This trend is depicted in Fig. 14b for the large model, where the maximum tilt angle of the facets is illustrated across various loading stages. For the case of $\nu = 0$, it is noticeable that cracks initiate at an approximate angle of 10° and gradually progress until they attain an angle of around $\phi_{\max} \approx 58°$. In the instance of $\nu = 0.45$, the initial angle starts at a lower value and gradually escalates to reach a plateau of 50°. Throughout these processes, the facets undergo coarsening, with smaller facets arresting at angles below 50°. Notably, in both cases, the hyperbolic fit yields a coefficient of determination exceeding 0.9, validating the converging behavior exhibited by the angles.

3.3.4. Apparent fracture toughness

Employing the model geometry and boundary conditions as depicted in Fig. 3 yields progressive initiation and propagation, requiring an increase in loading to advance the crack front. We have investigated the impact of Poisson's ratio on the critical loading point at which facets begin to manifest. Fig. 15 displays the normalized crack surface as a function of the normalized

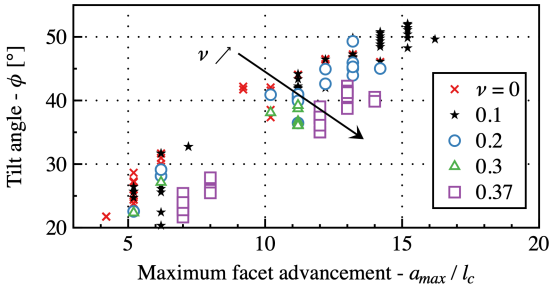

(a) Facet tilt angle as a function of crack advancement and Poisson's ratio in the small model with $R = 20l_c$ and $L = 200l_c$.

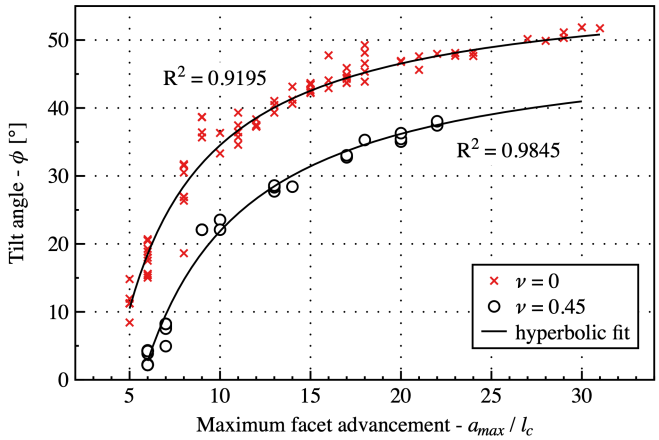

(b) Facet tilt angles as a function of the facets advancement. The results are fitted with the hyperbolic function: $\phi\left(a_{\max}\right) = \frac{\tilde{a}_{cr}}{a_{\max}/l_c} + \phi_{\max}$, where $\phi_{\max}$ donates the facet angle on the plateau. Results are plotted from various loading stages in the model with $R = 40l_c$ and $L = 200l_c$.

Figure 14: Effect of Poisson's ratio on the evolving tilt angle.

loading parameter. The loading necessary for horizontal propagation is determined through calculations without energy decomposition. With facets the damage field starts to increase at a loading significantly greater than that is expected for horizontal propagation. Interestingly, each case initiates at the same normalized value ($K_{\mathrm{III}}/k_{\mathrm{IIIc}} \approx 2.4$) independently of ν, indicating that a higher Poisson's ratio leads to a lower necessary stress at infinity (or its apparent stress intensity factor) due to the reduction in k_{IIIc} with an increase in ν (see eq. 1). As depicted in Fig. 11a, it is noteworthy that the ratio $g_c/(El_c)$ exhibits no influence on the curves illustrated in Fig. 15. The absence of any discernible impact can be attributed to the initial mother crack being infinitely larger than l_c, as a result, crack propagation follows Griffith's criterion.

During this initial period, the homogeneous damage forms around the original crack tip, which is represented in blue in Fig. 4. This period concludes when the cracks start to localize and facets form. As facet formation commences, the crack surface increases more rapidly with lower Poisson's ratios.

As suggested by Pham and Ravi-Chandar (2017), without imposing boundary conditions, the critical loading can only be assessed through a threshold in the newly formed crack surface. In this paper, to discuss critical loading in phase-field simulations, we will employ various threshold values in the relative crack advancement $\Delta a = \frac{S}{L}$ as a measure. For example, in Fig. 15 the red dashed line shows the normalized threshold of $\left.\frac{\Delta a}{l_c}\right|_{th} = 10$, where the normalized critical loading is $K_{\mathrm{III}}/k_{\mathrm{IIIc}} = 2.4$.

3.4. Contrast in modeling approaches

In contrast to initial phase-field models that lacked the formulation of Miehe et al. (2010a), our work distinguished between crack opening and closure through an energy decomposition scheme. This enabled the generation of facets in pure antiplane shear, in contrast to predictions of horizontal propagation by Pons and Karma (2010) and Chen et al. (2015).

Moreover, unlike the model presented by Pham and Ravi-Chandar (2017), our study reveals that without perturbation, the crack formed concentrically around the mother crack's front, extending beyond the initial crack plane. We employed a linear crack representation function (AT1 model) instead of the quadratic scheme and ensured damage irreversibility using Lagrange multipliers, deviating from Pham and Ravi-Chandar's approach. Additionally, we implemented an automatic time integration algorithm to control the time step, a detail not discussed in their paper. Furthermore, our study found no precise details about the energy decomposition scheme or the initial crack definition in the work of Pham and Ravi-Chandar (2017), which may explain the inability to initiate facets without significant defects.

3.5. Phase-field discussion and summary

In this section, we have demonstrated the proficiency of the phase-field approach in capturing the continuous formation of facets in pure antiplane shear. This accomplishment hinges on two key factors: (i) local toughness fluctuation and (ii) the spectral energy decomposition scheme. Notably, we showed that for a large range of reasonably small values of the Gaussian random field, the statistical results are independent of perturbations. This allows us to establish a link between the characteristic initiation distance between neighboring facets and the regularization scale of the phase-field model. Our study revealed that the initiation distance between facets is not influenced by the ratio $g_{\mathrm{mat}}/(El_c)$ but is proportional to the internal length-scale of the phase-field regularization and a Poisson's ratio-dependent function: $\Lambda = \tilde{\Lambda}_{\mathrm{PF}}(\nu) l_c$, with $\tilde{\Lambda}_{\mathrm{PF}}$ given in eq. (9). Furthermore, we emphasized the significance of positive and negative energy decomposition in inducing facets, suggesting that in fatigue experiments (Chen et al., 2015), potential contact and friction may play a crucial role in facet formation.

In our simulations we observed a gradual increase in the tilt angle of the facets as loading progressed. Detectable cracks initiated at around 5-10° and gradually propagated until reaching a maximum angle of 50-58°. During this process, the facets

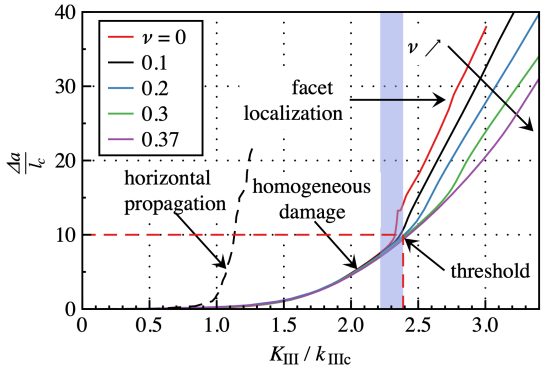

Figure 15: Normalized relative crack advancement as a function of the normalized loading. The period, where facets start to localize is highlighted in blue. The results for the case with no energy decomposition is displayed with the black dashed curve.

coarsened, and smaller ones stopped growing at angles below 50°. Similar trends were observed for different cases with varying Poisson's ratios, where the facets still initiated at a smaller angle and gradually increased towards 50°. Interestingly, this finding challenges the constant nature of the prediction made by Pollard et al. (1982). The discrepancy arises from the fact that Pollard et al. (1982) defines this angle based on the direction of the maximum opening stress, rather than on energetic considerations, as is the case with phase-field functions. It is worth noting that the finite size of the model, the limited distance between large facets and the boundary could potentially impact the facet angle on the plateau.

Furthermore, the findings indicated that crack initiation occurs at a loading level higher that which is associated with horizontal propagation. Interestingly, by increasing Poisson's ratio the load at which damage initiates decrease. In this aspect, facet formation aligns with Irwin's predictions used for horizontal propagation. Initially, homogeneous damage formed around the crack tip, followed by localization and facet formation. Finally, facet formation led to a more rapid increase in crack surface with lower Poisson's ratios.

The numerical experiments presented here are novel as they showcase facet initiation in a nearly pristine sample without any initial major defects or perturbations affecting the crack pattern. This discovery supports the idea that the emerging crack pattern is of physical significance, and its statistical properties are independent of the perturbations used. Consequently, the need for a regularization length is crucial because, for a vanishing l_c, the facet distance reduces to zero as well. Therefore, the experimental existence of facets suggests the existence of regularization as well.

Nevertheless, we encountered challenges in extracting a discrete quantity such as the characteristic initiation distance from phase-field models. This is due to the gradual branching of the mother crack into daughter cracks and the diffuse nature of the phase-field as a damage model. The initially regularized crack front obscures an eventual discrete transition, rendering it challenging to determine the precise facet distance at the point of initiation. In order to address these concerns, we proceed with our analysis using the coupled criterion. Unlike the phase-field model, re-initiation in the coupled criterion is discrete, and the facet distance becomes evident and independent of the size of the model. Building upon our previous successful comparison of 2D cases (Molnár et al., 2020a), we now extend our comparisons to 3D cases. Specifically, we aim to investigate the relationship between the regularization length used in phase-field models and the tensile strength in the 3D scenario.

4. Coupled criterion

The coupled criterion (Leguillon, 2002) is a widely used tool that combines an energy condition with a stress-based comparison. This combination naturally leads to the emergence of a characteristic length. Essentially, the theory states that for a crack to propagate, both energy and stress criteria must be satisfied at the same increment surface. In most cases, kinetic dissipation is neglected, and quasi-static conditions are assumed.

The energy criterion is based on the incremental energy release rate. which is determined by balancing the states before and after a finite size crack formation and was calculated as follows:

$$G(S_0 + \Delta S, P) = -\frac{\Pi^{int}(S_0 + \Delta S, P) - \Pi^{int}(S_0, P) - \Delta\Pi^{ext}(P)}{\Delta S}. \tag{10}$$

In this equation, Π^{int} represents the elastic strain energy, $\Delta\Pi^{ext}$ is the external work and P refers to the applied Dirichlet or Neumann boundary conditions. The term S_0 denotes the initial size of the crack surface, and ΔS is the unknown crack increment. The criterion asserts that a crack can open if the energy released from the elastic body exceeds the critical energy (g_{mat}) required to open the specific finite crack surface:

$$G(S_0 + \Delta S, P) \geq g_{\mathrm{mat}}. \tag{11}$$

The stress criterion, on the other hand, is the second requirement for crack propagation. It states that the stress perpendicular to the crack's opening direction along the expected crack path exceeds the material's tensile strength (σ_c) from a certain point onward:

$$\sigma_\theta\left(S_0 + s, P\right) \geq \sigma_c, \forall\ 0 \leq s \leq \Delta S. \tag{12}$$

While the energy criterion sets a minimum crack surface increment for crack initiation (assuming that G increases monotonously), the stress criterion establishes a maximum value due to the singular stress field at the crack tip. To satisfy both criteria simultaneously, the load is increased until the initiation increment provided by the energy criterion decreases and matches the increment along the crack path on which the stress criterion is satisfied. The main conclusion of the coupled criterion is that a finite crack increment ΔS is abruptly created at initiation to satisfy both the strength and energy requirements.

As a consequence, the coupled criterion enables us to investigate only the unstable cases where the incremental energy release rate increases with crack opening, while it reverts to Griffith's original solution in stable cases and the finite crack increment vanishes.

The coupled criterion is employed in this context to ascertain the initiation of planar facets, as illustrated in Fig. 2c. Once the shape of the daughter cracks is delineated, it is characterized by three parameters: (i) spacing (Λ), (ii) extent (ΔS), and (iii) rotation angle (ϕ). The coupled criterion, however, provides only two of the three necessary equations. Consequently, a decision was made to set the inclination angle at a fixed value of $\phi = 45°$, as it yields a shape closest to experimental observations. The focus will then be on determining Λ and ΔS at the onset of facet formation.

4.1. Stress criterion and proposed crack shape

The main challenge in implementing the coupled criterion is to identify an appropriate parameter space that accurately describes the crack opening and satisfies both the energy and stress criteria.

As suggested by previous studies (Leguillon, 2014; Doitrand and Leguillon, 2018a), the crack path can be determined by analyzing the stress isocontours around the mother crack in the absence of segments, which establishes a lower bound for surface

opening. To calculate the tensile stress at a specific point in infinite space, we utilized the analytic, singular solution derived from an elastic body (Westergaard, 1939) with a large mother crack: $r \ll a_0$ (where a_0 is the initial length of the mother crack):

$$\sigma_\theta\left(r,\theta,\phi\right) = \frac{K_{\mathrm{III}}}{\sqrt{2\pi r}} \cos\left(\frac{\theta}{2}\right) \sin\left(2\phi\right), \tag{13}$$

where the stress is characterized in a polar coordinate system, utilizing the parameters of distance (r), angle (θ), and inclination (ϕ) of the crack plane, as illustrated in Fig. 16[4]. Cracks are likely to form in regions where $\sigma_\theta \geq \sigma_c$. This domain can be represented by an isosurface, which outlines a specific region in space where crack opening becomes possible.

To maintain consistency with the fundamental assumption of the coupled criterion and for simplicity, we assume the instantaneous formation of a planar crack. Therefore, we need to define a two-dimensional surface within the envelope of the isosurface. To achieve this, we choose the intersection of the isosurface $\sigma_\theta = \sigma_c$ and a plane inclined around the x axis by an angle of $\phi = 45°$, where the tensile opening stress is maximum. This intersection defines a contour, as depicted in Fig. 16, where $\sigma_\theta \geq \sigma_c$. We will refer to this surface as our idealized representation of crack opening. The area of this surface can be represented in a dimensionless form using the following equation:

$$\frac{K_{\mathrm{III}}}{\sigma_c \sqrt[4]{\Delta S}} = c(\phi). \tag{14}$$

Here, the value of c, calculated numerically for $\phi = 45°$, is found to be approximately 2.207.

From a qualitative point of view, this shape is similar to that observed experimentally by Pham and Ravi-Chandar (2016) and it is close to the ones shown by phase-field simulations. Therefore, it seemed a reasonable choice.

The above crack shape enables us to characterize the opening of the crack using two variables: (i) the surface area of the crack (ΔS), and (ii) the distance between adjacent crack segments (Λ).

4.2. Incremental energy release rate

For mode III loading, the stress field is already available, but the incremental energy release rate for the specified crack opening needs to be determined as a function of the crack parameters (ΔS, Λ). For this, a series of linear calculations were

[4]Note, that r, θ and ϕ are not spherical coordinates in our case.

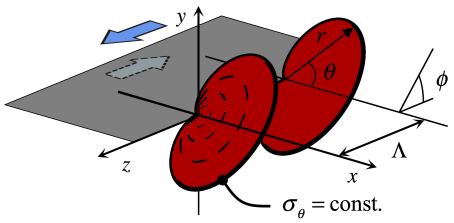

Figure 16: Idealized crack shape illustrating the coupled criterion, with the applied coordinate system.

carried out using the finite element method. To minimize the size effect, in order to be close to the problem of the infinite domain (see Fig. 2), the radius of the model was set to $R = 20x_{\max}$, where $x_{\max}$ represents the largest extent of the newly opened crack in the x direction. We choose $h_{\mathrm{CC}} = x_{\max}/50$ the smallest element size. It is worth noting that increasing the ratio by a factor of two between the smallest finite element size and the model size led to a difference of less than 1% in the energy release rate. The extent of the model in the z direction, and thus the characteristic spacing Λ was set to $100h_{\mathrm{CC}}$. To model periodic overlapping crack fronts, the sides of the model were tilted by ϕ, as previously suggested (Doitrand and Leguillon, 2018b; Lazarus et al., 2020; Doitrand et al., 2023). The finite element mesh was uniformly refined in the circular zone where the crack was present, using a linear hexahedral mesh. The displacement boundary conditions were set to match those used in the phase-field study (see eq. 6).

To calculate the energy release rate G, we computed the potential energy values while gradually increasing the crack opening ΔS. To minimize the effects of mesh fluctuations, the same finite element mesh was used consistently, regardless of the crack size. Fig. 17 presents the normalized incremental energy release rate as a function of the normalized crack surface. The normalization was made with the energy release rate value associated with rectilinear propagation and the load K_{III}:

$$G_0 = \frac{{K_{\mathrm{III}}}^2(1+\nu)}{E}. \tag{15}$$

Considering dimensional considerations, $\tilde{G} = G/G_0$ is exclusively dependent on ν and the normalized crack surface:

$$\Delta\tilde{S} = \Delta S/\Lambda^2, \tag{16}$$

given the infinite nature of the modeled domain.

Fig. 17 reveals that $\tilde{G}$ initially increases until it reaches a local maximum, denoted by $\tilde{G}_{\max}$, which occurs at a normalized crack surface of $\Delta\tilde{S}_{\max}$, before decreasing thereafter. $\tilde{G}_{\max}$ and $\Delta\tilde{S}_{\max}$ corresponds to the normalized state when the facet nucleates.

We observed that the maximum value of the normalized energy release rate ($\tilde{G}_{\max}$) is significantly lower than 1, facets releases only 13.5 % of the relative energy compared to horizontal propagation. This is consistent with previous findings of Mittelman and Yosibash (2015).

Finding a smaller G compared to horizontal propagation is interesting as it explains the difference in the apparent toughness observed as a function of energy decomposition splits in phase-field fracture (see Fig. 15). Because G, when facets nucleate, is lower, the crack propagation starts at a higher K_{III}. This observation is in good correspondence to mixed-mode I+III experiments (Hattali et al., 2021) too.

In order to compare our results with those obtained from the phase-field study, we present in Fig. 18 the maximum energy release rate and the corresponding surface opening as a function of Poisson's ratio. As shown in the figure, we observe a gradual decrease in $\tilde{G}_{\max}$ as the Poisson's ratio increases. The position where the maximum $\tilde{G}_{\max}$ is observed appears to peak around

$\nu = 0.35$.

4.3. Results of the coupled criterion

The main objective of this section is to determine the characteristic initiation distance between neighboring facets, Λ and the critical loading (K_{III}^{cr}), for a given set of parameters. Since $\tilde{G}_{\max}$ is independent of the initiation distance, we can use it to determine the critical load for a given Poisson's ratio. The energy release rate at the facet initiation can be obtained from the following equation:

$$G = G_0 \tilde{G}_{\max}(\nu) = \frac{K_{\mathrm{III}}^2 (1+\nu)}{E} \tilde{G}_{\max}(\nu). \tag{17}$$

By equating G to the materials fracture toughness, g_{mat}, we obtain the critical loading:

$$K_{\mathrm{III}}^{cr} = \sqrt{\frac{E g_{\mathrm{mat}}}{\hat{G}_{\max}(\nu)(1+\nu)}}. \tag{18}$$

Substituting the critical loading into eq. (14), we get the surface area where the stress criterion for initiation is satisfied, which we denote as $\Delta S_{\sigma}^{cr}(K_{\mathrm{III}}^{cr}, \sigma_c)$, and where $\sigma_\theta \geq \sigma_c$. Finally, utilizing the position of the normalized crack surface $\Delta \tilde{S}_{\max}(\nu)$ from equation (16), we can determine the characteristic facet distance:

$$\Lambda = \sqrt{\frac{\Delta S_{\sigma}^{cr}(K_{\mathrm{III}}^{cr}, \sigma_c)}{\Delta \tilde{S}_{\max}(\nu)}}. \tag{19}$$

The primary objective is to identify material parameters that affect the initiation distance. By combining eq. (14), (18), and (19), we establish a correlation where E, g_{mat}, σ_c, and ν are the principal variables. From this equation, l_{mat} (as seen in eq. 2) can be extracted, leading to the following correlation for pure antiplane shear:

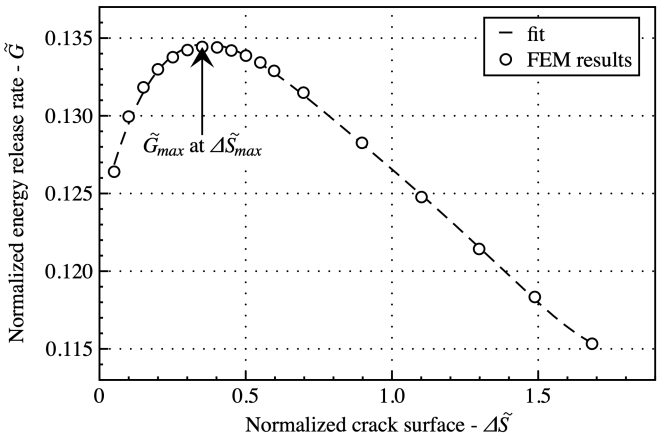

Figure 17: Normalized incremental energy release rate as a function of normalized crack opening for $\nu = 0.37$. The arrow points to the maximum value $\tilde{G}_{\max}$ at the normalized surface opening $\Delta\tilde{S}_{\max}$.

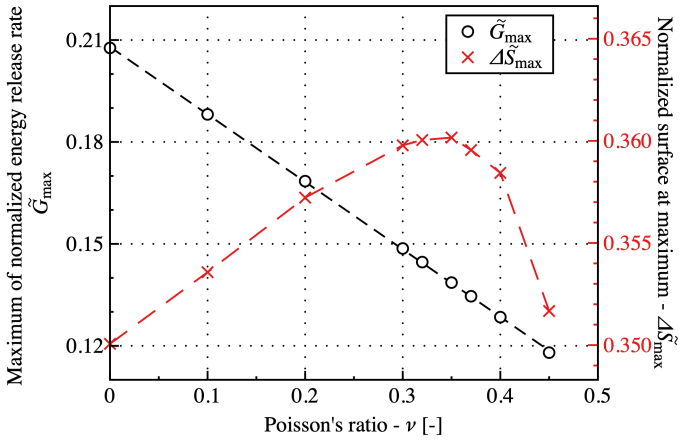

Figure 18: Maximum of the normalized energy release rate and the related normalized surface opening as a function of Poisson's ratio for $\phi = 45°$. The curves are guide to the eye.

$$\frac{\Lambda}{l_{\text{mat}}} = \frac{1}{(1+\nu)\tilde{G}_{\max}(\nu)c^2\sqrt{\Delta\tilde{S}_{\max}(\nu)}} \equiv \tilde{\Lambda}_{\text{CC}}(\nu)\,, \tag{20}$$

where $\tilde{G}_{\max}$, and $\Delta\tilde{S}_{\max}$ are dimensionless constants only influenced by Poisson's ratio and c is a coefficient linking the loading and σ_c to the newly opened surface (see eq. 14). Based on these findings, it becomes evident that the characteristic initiation distance between facets is linked to the material's intrinsic length and affected solely by Poisson's coefficient. Interestingly, the finding that the initiation distance is unaffected by $g_{\text{mat}}/(El_{\text{mat}})$ aligns remarkably well with the phase-field results.

Furthermore, similarly to phase-field simulations (as shown in Fig. 15), the critical loading can be normalized using Irwin's prediction for horizontal propagation (see eq. 1), to obtain the following dimensionless form:

$$\frac{K_{\text{III}}^{cr}}{k_{\text{IIIc}}} = \frac{1}{\sqrt{\tilde{G}_{\max}(\nu)}}. \tag{21}$$

5. Discussion

In Griffith's original theory, the ratio g_{mat}/E also delineates a characteristic length. However, through our comprehensive analysis employing both methodologies, we have demonstrated that the initiation distance between facets remains unaffected by this ratio. As elucidated in our recent investigation of mode I and II cracking (Molnár et al., 2020a), the influence of the g_{mat}/E ratio becomes pronounced when a finite mother crack length (a_0) is introduced, particularly as a_0 approaches the characteristic material length (l_{mat}) or the phase-field length (l_c). Conversely, when a_0 significantly surpasses these material lengths, their impact becomes negligible.

In the present study, the effect of g_{mat}/E remains invisible due to boundary conditions reflecting cases where a_0 is infinitely greater than both the model size and the material's characteristic lengths. However, we anticipate that simulations modeling

cases where a_0 is comparable to l_c would unveil discernible effects of g_{mat} and E.

Furthermore, our investigation has shown that both the coupled criterion and the phase-field method are effective in analyzing crack front segmentation in pure antiplane shear. Both methods indicate that the characteristic distance between daughter cracks is proportional to the internal length and depends only on ν. Therefore, for a meaningful comparison of results from these two methods, it is crucial to establish a correlation between l_c and l_{mat}:

$$l_c = \eta^2 l_{\mathrm{mat}}. \tag{22}$$

In our recent publications (Molnár et al., 2020a; Molnár et al., 2022), we have demonstrated that the η parameter can be obtained from the homogeneous phase-field solution by comparing the maximum tensile stress to the tensile strength of the material:

$$\eta = \eta_{\mathrm{homo}}\left(\frac{\sigma_2}{\sigma_1}, \frac{\sigma_3}{\sigma_1}, \nu\right), \tag{23}$$

where η_{homo} is a scalar variable that takes into account the effect of the stress state. More precisely, the application of the phase-field technique and the coupled criterion to a 3D domain uniformly stressed by σ_1, σ_2, and σ_3 (representing the principal stresses) enables us to establish a link between the two length scales. For example, in a pure shear where all stress components except τ_{yz} are zero, the ratios of principal stresses are $\frac{\sigma_2}{\sigma_1} = 0$ and $\frac{\sigma_3}{\sigma_1} = -1$. This yields $\eta = 0.51$ for $\nu = 0.45$ for the AT1 phase-field model. The value of η can be calculated using an iterative algorithm for other stress states and Poisson's ratios using the method explained by Molnár et al. (2020a) and Molnár et al. (2022).

In the first step (in Section 5.1), we selected $\eta = \eta_{\mathrm{homo}}$ and compared the results to the experiments presented by Knauss (1970). Subsequently, in the second step (in Section 5.2), we explored the possibility of redefining η to align the values of Λ obtained by the phase-field simulations and the coupled criterion.

5.1. Characteristic initiation distance between facets in Solithane

Since the length scale is represented differently in both methods, we will compare the results for a specific material with which experiments were conducted. Unfortunately, pure mode III experiments are scarce and the crack pattern might be affected by the finite size of the specimen. Nevertheless, this comparison will provide a qualitative validation of the method. In one of the earliest experimental papers studying mode III fracture (Knauss, 1970), Solithane 113 (50/50) was used. This transparent polymer is easy to work with, with a relatively small Young's modulus that varies between $E = 3.00 - 4.14$ MPa (Hearne and Kubitza, 1969) and a Poisson's ratio close to incompressibility. We will approximate the Poisson's ratio as $\nu = 0.45$ based on the study published by Hearne and Kubitza (1969). The critical energy release rate at ambient temperature was found to be between $g_{\mathrm{mat}} = 67.8 - 113.0$ J/m^2 (Mueller and Knauss, 1971), and the tensile strength was $\sigma_c = 2.85$ MPa. In this study, we will consider the material to be linearly elastic and ideally brittle.

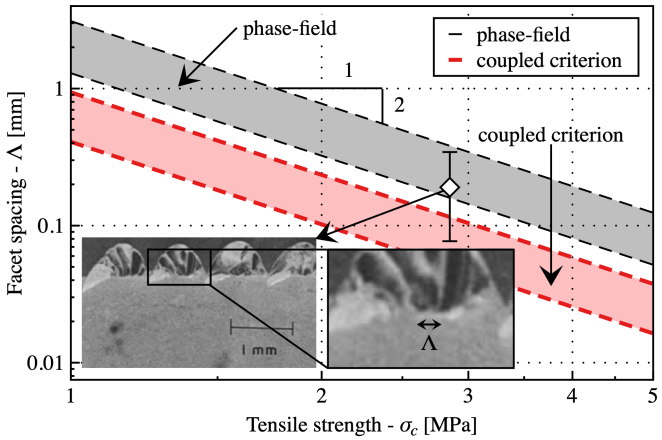

Figure 19: Characteristic initiation distance between neighboring facets as a function of tensile strength in double logarithmic scale. The numerical results are shown for a range of material properties ($E = 3.00 - 4.14$ MPa, $\nu = 0.45$, $g_{\text{mat}} = 67.8 - 113.0$ J/m^2). Experimental results shown in the inset are taken from Knauss (1970). The error bars represent 95% percentiles.

For Solithane 113 (50/50), the regularization phase-field length is not known experimentally. Therefore, we will approximate this quantity using the combination of equations (2) and (22), suggesting that the internal length, and hence the characteristic localization distance, can be approximated by the following equation:

$$\Lambda_{\text{PF}} \approx \tilde{\Lambda}_{\text{PF}}(\nu)\, l_c = \tilde{\Lambda}_{\text{PF}}(\nu)\, \eta_{\text{homo}}^2 \frac{E g_{\text{mat}}}{\sigma_c^2}. \tag{24}$$

where $\tilde{\Lambda}_{\text{PF}}(\nu)$ can be obtained from eq. (9), and η_{homo} is discussed in eq. (23).

We recall that the initiation distance between neighboring facets in the coupled criterion can also be determined from Irwin's length in eq. (2) and the dimensionless parameters presented in Fig. 18:

$$\Lambda_{\text{CC}} = \tilde{\Lambda}_{\text{CC}}(\nu)\, l_{\text{mat}} = \tilde{\Lambda}_{\text{CC}}(\nu) \frac{E g_{\text{mat}}}{\sigma_c^2}. \tag{25}$$

For comparison, Fig. 19 demonstrates the variation of the characteristic initiation distance as a function of σ_c for the given range of material parameters. The gray area represents the phase-field prediction based on eq. (24), while the red area represents the results of the coupled criterion (see eq. 25). This graph provides valuable insights into the relationship between σ_c and the characteristic initiation distance.In Fig. 19, we have highlighted the experimental measurements of Knauss (1970), where we counted all the small ridges present in their results shown in Fig. 2 of the aforementioned paper. Based on our analysis, we made the assumption that the smallest localization distance corresponds to the initial series of facets. These facets subsequently merge together, forming a second series of cracks, as emphasized in the paper. It is worth noting that, similar to the phase-field simulations, determining the precise initiation distance between daughter cracks in experiments is a challenging task; one could argue that the first localization corresponds to the larger, fin-like shapes.

Despite the inherent difficulty in defining the initiation distance in experiments, our findings indicate an average distance

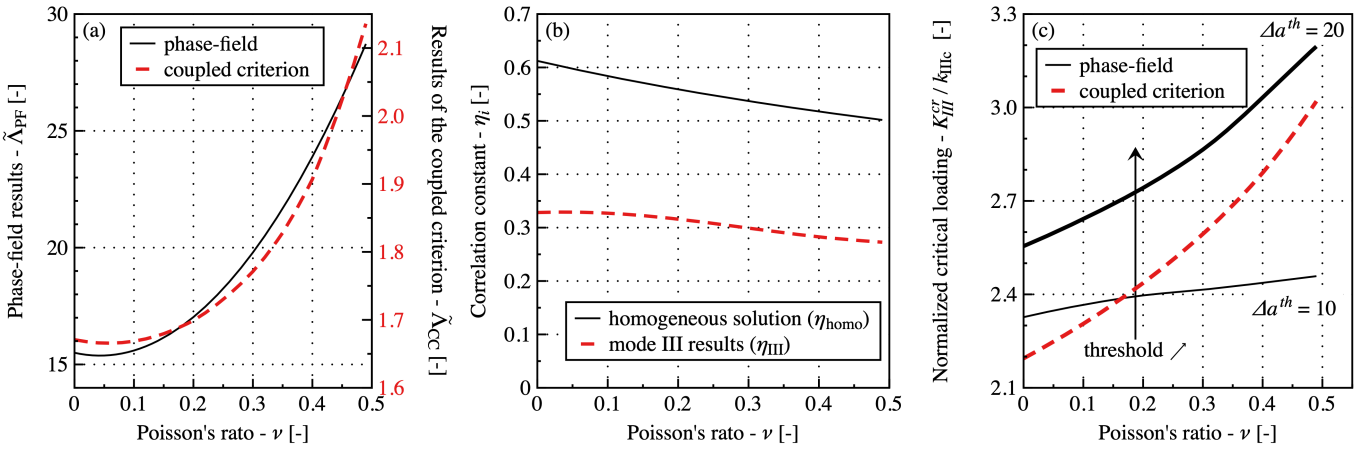

Figure 20: (a) Normalized initiation distance; (b) correlation constant η_i; and (c) critical loading as a function of Poisson's ratio.

between neighboring facets at initiation of 0.19 mm, which exhibits a remarkable correlation with the predictions of both methods. While the phase-field prediction aligns more closely with the range of experimental measurements, the coupled criterion also yields a comparable set of results.

5.2. Influence of Poisson's ratio

To evaluate the influence of Poisson's ratio on the initiation distance between facets, we presented functions (9) and (20) in Fig. 20a. The figure illustrates that both results exhibit similar trends. Both methods predict a minimum within the range of $\nu = [0; 0.1]$, followed by a monotonous increase. However, the exact values differ by an order of magnitude, attributed to the utilization of different normalization length scales.

In equation (22), we established the correlation between l_c and l_{mat} based on the maximum tensile stress in the homogeneous solution. This correlation can also be established based on the facet distance:

$$\eta_{\mathrm{III}} = \sqrt{\frac{\tilde{\Lambda}_{\mathrm{CC}}}{\tilde{\Lambda}_{\mathrm{PF}}}}. \tag{26}$$

Fig. 20b displays the correlation constants as a function of Poisson's ratio. The values exhibit a similar trend, decreasing as Poisson's ratio increases. There seems to be a consistently maintained difference of approximately $\eta_{\mathrm{III}} = 0.55\eta_{\mathrm{homo}}$ between the two definitions. Notably, the correlation presented in eq. (22) exhibited slightly better performance for mode I and II loading cases. This variation in values is likely attributed to the fact that, in mode I and II, the crack path remained consistent. While, in mode III, the form of the newly formed fracture was slightly different since in the phase-field model the crack developed in a continuous fashion, whereas in the coupled criterion we assumed an discrete opening. Nonetheless, it is intriguing that a single correlation can be established for a complex loading case based on only three material parameters. This result suggests that, by conducting mode III fragmentation experiments, the value of l_c for a given material can be confidently estimated by counting the facets at initiation.

In Fig. 20c, the critical loading is presented as a function of Poisson's ratio. The red dashed curve was obtained using eq. (18). Results from the coupled criterion show an increase as the parameter ν rises. In the phase-field calculations, two distinct stages are evident: the loading when the crack starts to propagate and when the facets appear, as illustrated in Fig. 15. Therefore, different threshold values of Δa^{th} were used to study the critical loading. The smaller value corresponds to the point where facets start to form, while the higher one corresponds to when facets are clearly visible. Beyond $\Delta a^{th} = 20$, the phase-field results exhibit similar tendencies to the coupled criterion. This is not surprising, as the coupled criterion promptly considers larger facets when the interaction between facets becomes significant. Nevertheless, the critical loading values obtained from both techniques are relatively close between the two methods.

6. Conclusion

The paper offers a comprehensive numerical analysis of daughter crack formation in pure antiplane shear. We developed innovative phase-field models that induced an instability by the spatial variations of the critical energy release rate. This was achieved through a semi-periodic Gaussian random field. We thoroughly examined the impact of numerical and material parameters on the newly formed daughter cracks' shape and spacing. Additionally, we conducted an investigation based on the coupled criterion to explain the observed phenomena. By considering the initiations' angle, we determined the fin-shaped crack surface based on opening stresses. Employing both techniques, we probed the material parameters' effect on the critical loading and characteristic spacing between facets.

Traditionally, in phase-field studies, the length scale parameter has been regarded as a trade-off that could potentially distort the mechanical behavior of fracture problems while enabling variational approaches. However, in this paper, with both techniques, we linked the initiation distance between neighboring facets to the material's internal length scales. This challenges the traditional assumption, as without a length scale, finite facet formation is not feasible. Consequently, we have demonstrated that the inclusion of a length scale parameter helps us to model more complex fracture phenomena.

In the phase-field study, we discovered that localization is achieved through the deviatoric component of the asymmetric energy decomposition. While experimenting with Poisson's ratio, we observed a significant alteration in the crack form and spacing. When reducing Poisson's ratio, the facet spacing reduced. Furthermore, the crack pattern remained relatively constant as we tinkered with the Gaussian random field. Astonishingly, neither the mean fracture toughness nor Young's modulus bore any significant impact. Our results revealed that the facets initiate at a small angle and deviate from the horizontal mother crack gradually. We found that facets coarsen until they reach approximately 50°.

In order to elucidate the phenomenon of localization evident in the phase-field model, we approached the problem through the lens of the coupled criterion. Employing finite element calculations, we were able to observe a progressive increase in the energy release rate until reaching a peak, after which a gradual decline was detected.

Upon comparing the results of the two methods, we noted similar initiation distances between daughter cracks to experimental measurements of Knauss (1970). We have shown that the tendencies as a function of tensile strength are identical between the

two methods. We found that in both methods, the effect of Poisson's ratio was similar. This finding aligns well with our previous conclusions (Molnár et al., 2020a). Additionally, we demonstrate that the measurement of facet spacing in antiplane shear provides a potential estimate of the regularization length scale used in phase-field simulations.

Notwithstanding their significance, the findings presented in this paper prompt several inquiries that warrant further investigation. Foremost, it is crucial to develop a reliable experimental method to measure initiation angles and track the continuous formation of cracks under pure mode III loading conditions. Moreover, an enhanced model for the coupled criterion, inspired by the phase-field regularization, incorporating a non-singular, regularized stress field is essential. This approach would enable the coupled criterion to address stable initiation cases and provide the third equation necessary to determine the initiation angle accurately. Additionally, phase-field simulations and coupled criterion models should be employed to test mixed mode I+III conditions, consider realistic boundary conditions, assess the impact of crack tip radius, and investigate the effects of a realistically inhomogeneous material. Furthermore, a detailed analysis utilizing configurational forces (Yan et al., 2023) could potentially shed light on the physical interpretation of the regularization length and elucidate the interaction between facets.

Acknowledgment

The authors extend their deepest gratitude to the late Dominique Leguillon for all the stimulating discussions and invaluable guidance throughout the course of this work and in their lives. His insights and unwavering passion for scientific will forever serve as a profound source of inspiration. This research was funded, in part, by French Research National Agency program GaLAaD (ANR-20-CE08-0002). A CC-BY public copyright license has been applied by the authors to the present document and will be applied to all subsequent versions up to the Author Accepted Manuscript arising from this submission, in accordance with the grant's open access conditions.

Alsaadi, M., Erkliğ, A., Bulut, M., 2018. Mixed-mode I/III fracture toughness of polymer matrix composites toughened with waste particles. Science and Engineering of Composite Materials 25 (4), 679–687.

Ambati, M., Gerasimov, T., Lorenzis, L. D., 2015. Phase-field modeling of ductile fracture. Computational Mechanics 55 (5), 1017–1040.

Ambrosio, L., Tortorelli, V. M., 1990. Approximation of functional depending on jumps by elliptic functional via t-convergence. Communications on Pure and Applied Mathematics 43 (8), 999–1036.

Amestoy, M., Leblond, J. B., 1992. Crack paths in plane situations—II. detailed form of the expansion of the stress intensity factors. International Journal of Solids and Structures 29 (4), 465–501.

Bernard, P.-E., Moës, N., Chevaugeon, N., 2012. Damage growth modeling using the thick level set (TLS) approach: Efficient discretization for quasi-static loadings. Computer Methods in Applied Mechanics and Engineering 233, 11–27.

Bonniot, T., Doquet, V., Mai, S., 2018. Mixed mode II and III fatigue crack growth in a rail steel. International Journal of Fatigue.

Bourdin, B., Francfort, G., Marigo, J.-J., 2000. Numerical experiments in revisited brittle fracture. Journal of the Mechanics and Physics of Solids 48 (4), 797 – 826.

Bourdin, B., Francfort, G. A., Marigo, J.-J., 2008. The Variational Approach to Fracture. Springer Netherlands.

Buckingham, E., 1914. On physically similar systems; illustrations of the use of dimensional equations. Physical review 4 (4), 345.

Cahn, J. W., Hilliard, J. E., 1958. Free energy of a nonuniform system. i. interfacial free energy. The Journal of Chemical Physics 28 (2), 258–267.

Cambonie, T., Klinger, Y., Lazarus, V., 2019. Similarities between mode III crack growth patterns and strike-slip faults. Philosophical Transactions of the Royal Society A: Mathematical, Physical and Engineering Sciences 377 (2136), 20170392.

Campagnolo, A., Sapora, A., 2021. A FFM analysis on mode III static and fatigue crack initiation from sharp v-notches. Engineering Fracture Mechanics 258, 108063.

Chen, C.-H., Cambonie, T., Lazarus, V., Nicoli, M., Pons, A. J., Karma, A., 2015. Crack front segmentation and facet coarsening in mixed-mode fracture. Physical Review Letters 115 (26), 265503.

Citarella, R., Buchholz, F.-G., 2008. Comparison of crack growth simulation by DBEM and FEM for sen-specimens undergoing torsion or bending loading. Engineering Fracture Mechanics 75 (3-4), 489–509.

Cooke, M. L., Pollard, D. D., 1996. Fracture propagation paths under mixed mode loading within rectangular blocks of polymethyl methacrylate. Journal of Geophysical Research 101 (B2), 3387–3400.

Cox, S. J. D., Scholz, C. H., 1988. On the formation and growth of faults: an experimental study. Journal of Structural Geology 10 (4), 413–430.

Dietrich, C. R., Newsam, G. N., 1997. Fast and exact simulation of stationary gaussian processes through circulant embedding of the covariance matrix. SIAM Journal on Scientific Computing 18 (4), 1088–1107.

Doitrand, A., Leguillon, D., 2018a. 3D application of the coupled criterion to crack initiation prediction in epoxy/aluminum specimens under four point bending. International Journal of Solids and Structures 143, 175–182.

Doitrand, A., Leguillon, D., 2018b. Numerical modeling of the nucleation of facets ahead of a primary crack under mode I+III loading. International Journal of Fracture 213, 37–50.

Doitrand, A., Leguillon, D., Molnár, G., Lazarus, V., 2023. Revisiting facet nucleation under mixed mode I+III loading with T-stress and mode-dependent fracture properties. International Journal of Fracture 242, 85–106.

Erdogan, F., Sih, G. C., 1963. On the crack extension in plates under plane loading and transverse shear. Journal of Basic Engineering 85, 519–525.

Faria Ricardo, L. F., Leguillon, D., Parry, G., Doitrand, A., 2020. Modeling the thermal shock induced cracking in ceramics. Journal of the European Ceramic Society 40 (4), 1513–1521.

Fonte, M., Reis, L., Romeiro, F., Li, B., Freitas, M., 2006. The effect of steady torsion on fatigue crack growth in shafts. International Journal of Fatigue 28 (5), 609–617, selected papers from the 7th International Conference on Biaxial/Multiaxial Fatigue and Fracture (ICBMFF).

Francfort, G., Marigo, J.-J., 1998. Revisiting brittle fracture as an energy minimization problem. Journal of the Mechanics and Physics of Solids 46 (8), 1319 – 1342.

Ginzburg, V. L., Landau, L. D., 1950. On the theory of superconductivity. J. Exptl. Theoret. Phys. (U.S.S.R) 20, 1064.

Goldstein, R., Osipenko, N., 2012. Fracture structure near a longitudinal shear macrorupture. Mechanics of Solids 47, 505–516.

Gravouil, A., Moës, N., Belytschko, T., 2002. Non-planar 3D crack growth by the extended finite element and level sets—part II: Level set update. International journal for numerical methods in engineering 53 (11), 2569–2586.

Griffith, A., 1924. The theory of rupture. In: First Int. Cong. Appl. Mech. pp. 55–63.

Griffith, A. A., 1921. The phenomena of rupture and flow in solids. Philosophical Transactions of the Royal Society of London A: Mathematical, Physical and Engineering Sciences 221 (582-593), 163–198.

Hattali, M. L., Cambonie, T., Lazarus, V., 2021. Toughening induced by the formation of facets in mode I+III brittle fracture: Experiments versus a two-scale cohesive zone model. Journal of the Mechanics and Physics of Solids 156, 104596.

Hearne, G. L., Kubitza, W. K., 1969. Experimental analysis of low profile flange connections final technical report. Tech. Rep. No. NASA-CR-98458, National Aeronautics and Space Administration.

Henry, H., 2016. Crack front instabilities under mixed mode loading in three dimensions. Europhysics Letters 114 (6), 66001.

Hull, D., 1994. The effect of mixed mode I/III on crack evolution in brittle solids. International journal of fracture 70, 59–79.

Irwin, G. R., 1957. Relation of stresses near a crack to the crack extension force. Proceedings of IXth International Congress of Applied Mechanics VIII, 245–251.

Irwin, R. G., 1958. Fracture. Springer Berlin Heidelberg, Berlin, Heidelberg, pp. 551–590.

761 Kachanov, L. M., 1958. Rupture time under creep conditions.

762 Knauss, W. G., 1970. An observation of crack propagation in anti-plane shear. International Journal of Fracture Mechanics 6 (2),
763 183–187.

764 Lang, A., Potthoff, J., 2011. Fast simulation of Gaussian random fields.

765 Lazarus, V., Buchholz, F.-G., Fulland, M., Wiebesiek, J., 2008. Comparison of predictions by mode II or mode III criteria on
766 crack front twisting in three or four point bending experiments. International journal of fracture 153 (2), 141–151.

767 Lazarus, V., Prabel, B., Cambonie, T., Leblond, J., 2020. Mode I+III multiscale cohesive zone model with facet coarsening and
768 overlap: Solutions and applications to facet orientation and toughening. Journal of the Mechanics and Physics of Solids 141,
769 104007.

770 Lebihain, M., Leblond, J.-B., Ponson, L., 2022. Crack front instability in mixed-mode I+III: The influence of non-singular
771 stresses. European Journal of Mechanics - A/Solids, 104602.

772 Leblond, J.-B., Karma, A., Lazarus, V., 2011. Theoretical analysis of crack front instability in mode I+III. Journal of the
773 Mechanics and Physics of Solids 59 (9), 1872–1887.

774 Leblond, J.-B., Karma, A., Ponson, L., Vasudevan, A., 2019. Configurational stability of a crack propagating in a material with
775 mode-dependent fracture energy - part I: Mixed-mode I+III. Journal of the Mechanics and Physics of Solids 126, 187–203.

776 Leblond, J.-B., Lazarus, V., Aug. 2015. On the strong influence of imperfections upon the quick deviation of a mode I+III crack
777 from coplanarity. Journal of Mechanics of Materials and Structures 10 (3), 299–315.

778 Leblond, J.-B., Lazarus, V., Karma, A., 2015. Multiscale cohesive zone model for propagation of segmented crack fronts in mode
779 I+III fracture. International Journal of Fracture 191, 167–189.

780 Leguillon, D., 2002. Strength or toughness? a criterion for crack onset at a notch. European Journal of Mechanics - A/Solids
781 21(1), 61–72.

782 Leguillon, D., 2014. An attempt to extend the 2d coupled criterion for crack nucleation in brittle materials to the 3D case.
783 Theoretical and Applied Fracture Mechanics 74, 7–17.

784 Leguillon, D., Yosibash, Z., 2003. Crack onset at a v-notch. influence of the notch tip radius. International journal of fracture
785 122, 1–21.

786 Lin, B., Mear, M. E., Ravi-Chandar, K., 2010. Criterion for initiation of cracks under mixed-mode I+III loading. International
787 journal of fracture 165, 175–188.

Linse, T., Hennig, P., Kästner, M., de Borst, R., 2017. A convergence study of phase-field models for brittle fracture. Engineering Fracture Mechanics 184, 307–318.

Lu, Y., Helfer, T., Bary, B., Fandeur, O., 2020. An efficient and robust staggered algorithm applied to the quasi-static description of brittle fracture by a phase-field approach. Computer Methods in Applied Mechanics and Engineering 370, 113218.

Martin, E., Leguillon, D., Seveček, O., Bermejo, R., 2018. Understanding the tensile strength of ceramics in the presence of small critical flaws. Engng. Fract. Mech. 201, 167–175.

McClintock, F. A., Irwin, G. R., 1965. Plasticity aspects of fracture mechanics. In: E24, C. (Ed.), Fracture Toughness Testing and its Applications. ASTM International West Conshohocken, pp. 84–113.

Miehe, C., Welschinger, F., Hofacker, M., 2010a. Thermodynamically consistent phase-field models of fracture: Variational principles and multi-field FE implementations. International Journal for Numerical Methods in Engineering 83 (10), 1273–1311.

Mittelman, B., Yosibash, Z., 2015. Energy release rate cannot predict crack initiation orientation in domains with a sharp v-notch under mode III loading. Engineering Fracture Mechanics 141, 230–241.

Molnár, G., Doitrand, A., Estevez, R., Gravouil, A., 2020a. Toughness or strength? regularization in phase-field fracture explained by the coupled criterion. Theoretical and Applied Fracture Mechanics 109, 102736.

Molnár, G., Doitrand, A., Jaccon, A., Prabel, B., Gravouil, A., 2022. Thermodynamically consistent linear-gradient damage model in abaqus. Engineering Fracture Mechanics 266, 108390.

Molnár, G., Gravouil, A., Seghir, R., Réthoré, J., 2020b. An open-source abaqus implementation of the phase-field method to study the effect of plasticity on the instantaneous fracture toughness in dynamic crack propagation. Computer Methods in Applied Mechanics and Engineering 365, 113004.

Mueller, H. K., Knauss, W. G., 1971. The fracture energy and some mechanical properties of a polyurethane elastomer. Transactions of the Society of Rheology 15 (2), 217–233.

Mumford, D., Shah, J., 1989. Optimal approximations by piecewise smooth functions and associated variational problems. Communications on pure and applied mathematics 42 (5), 577–685.

Nikravesh, M. Y., Meidan-Sharafi, M., 2016. Failure of a steam turbine rotor due to circumferential crack growth influenced by temperature and steady torsion. Engineering Failure Analysis 66, 296–311.

Palaniswamy, K., Knauss, W., 1978. II - On the problem of crack extension in brittle solids under general loading. In: Mechanics Today. pp. 87–148.

Pandolfi, A., Li, B., Ortiz, M., 2013. Modeling fracture by material-point erosion. International Journal of fracture 184, 3–16.

Pham, K., Amor, H., Marigo, J.-J., Maurini, C., 2011. Gradient damage models and their use to approximate brittle fracture. International Journal of Damage Mechanics 20 (4), 618–652.

Pham, K. H., Ravi-Chandar, K., 2014. Further examination of the criterion for crack initiation under mixed-mode I+III loading. International Journal of Fracture 189 (2), 121–138.

Pham, K. H., Ravi-Chandar, K., 2016. On the growth of cracks under mixed-mode I+III loading. International Journal of Fracture 199 (1), 105–134.

Pham, K. H., Ravi-Chandar, K., 2017. The formation and growth of echelon cracks in brittle materials. International Journal of Fracture 206 (2), 229–244.

Pollard, D. D., Segall, P., Delaney, P. T., 1982. Formation and interpretation of dilatant echelon cracks. Geological Society of America Bulletin 93 (12), 1291–1303.

Pons, A. J., Karma, A., 2010. Helical crack-front instability in mixed-mode fracture. Nature 464 (7285), 85–89.

Raghavachary, S., Rosenfield, A. R., Hirth, J. P., 1990. Mixed mode I/III fracture toughness of an experimental rotor steel. Metallurgical Transactions A 21, 2539–2545.

Ronsin, O., Caroli, C., Baumberger, T., 2014. Crack front échelon instability in mixed mode fracture of a strongly nonlinear elastic solid. Europhysics Letters 105 (3), 34001.

Shi, F., Wang, D., Yang, Q., 2022. An XFEM-based numerical strategy to model three-dimensional fracture propagation regarding crack front segmentation. Theoretical and Applied Fracture Mechanics 118, 103250.

Sommer, E., 1969. Formation of fracture 'lances' in glass. Engineering Fracture Mechanics 1 (3), 539–546.

Tanné, E., Li, T., Bourdin, B., Marigo, J.-J., Maurini, C., 2018. Crack nucleation in variational phase-field models of brittle fracture. Journal of the Mechanics and Physics of Solids 110, 80–99.

Vaschy, A., 1892. Sur les lois de similitude en physique. In: Annales télégraphiques. Vol. 19. pp. 25–28.

Vasudevan, A., Ponson, L., Karma, A., Leblond, J.-B., 2020. Configurational stability of a crack propagating in a material with mode-dependent fracture energy – part II: Drift of fracture facets in mixed-mode I+II+III. Journal of the Mechanics and Physics of Solids 137, 103894.

Westergaard, H. M., 1939. Bearing pressures and cracks: Bearing pressures through a slightly waved surface or through a nearly flat part of a cylinder, and related problems of cracks.

Wu, J.-Y., 2018b. Robust numerical implementation of non-standard phase-field damage models for failure in solids. Computer Methods in Applied Mechanics and Engineering 340, 767 – 797.

Wu, J.-Y., Huang, Y., 2020. Comprehensive implementations of phase-field damage models in abaqus. Theoretical and Applied Fracture Mechanics 106, 102440.

Yan, S., Schlüter, A., Faust, E., Müller, R., 2023. Configurational forces in a phase field model for the cyclic fatigue of heterogeneous materials. Forces in Mechanics 13, 100239.

Yosibash, Z., Mittelman, B., 2016. A 3-D failure initiation criterion from a sharp v-notch edge in elastic brittle structures. European Journal of Mechanics - A/Solids 60, 70–94.

Younes, A. I., Engelder, T., 1999. Fringe cracks: key structures for the interpretation of the progressive Alleghanian deformation of the appalachian plateau. Geological Society of America Bulletin 111 (2), 219–239.

Zimmermann, E. A., Launey, M. E., Barth, H. D., Ritchie, R. O., 2009. Mixed-mode fracture of human cortical bone. Biomaterials 30 (29), 5877–5884.

Appendix A. Effect of phase-field model parameters

We conducted additional experiments to investigate the impact of model parameters on crack patterns. Fig. A.21 presents the results of varying σ_G and its gradual effect on the crack pattern. Notably, we observed that decreasing σ_G delays the localization of the cracks. However, upon closer inspection, we found that even when $\sigma_G = 10^{-7} g_c$, the facets still localized at the same position. Based on our observations, we concluded that the magnitude of σ_G does not affect the distance between facets.

We also conducted additional tests by generating the Gaussian random field using different random seeds. The results are presented in Fig. A.22, which clearly shows that the facets localize at different positions for each seed, but the characteristic distance between the facets remained similar across all examples.

Fig. A.23 depicts the effect of the radius of the finite element model on the crack pattern formation. Our observations indicate that when the radius was sufficiently large ($R \leq 20 l_c$), the localization of the facets was not affected. However, if the radius was smaller, we obtain a homogeneous, phenomenological-like response without any localization. Conversely, if the radius was larger, we observed that the initial localization around the mother crack tip was reduced, and the facets became more visible.

Fig. A.24 demonstrates the influence of the finite element size on both the crack pattern and the characteristic distance. Our observation led us to conclude that the effect is relatively insignificant. Specifically, we found that the characteristic initiation distance remained unchanged. The only noticeable distinction was that the facet, which arrested the most rapidly at the left boundary, exhibited a slightly greater propagation before coming to a halt.

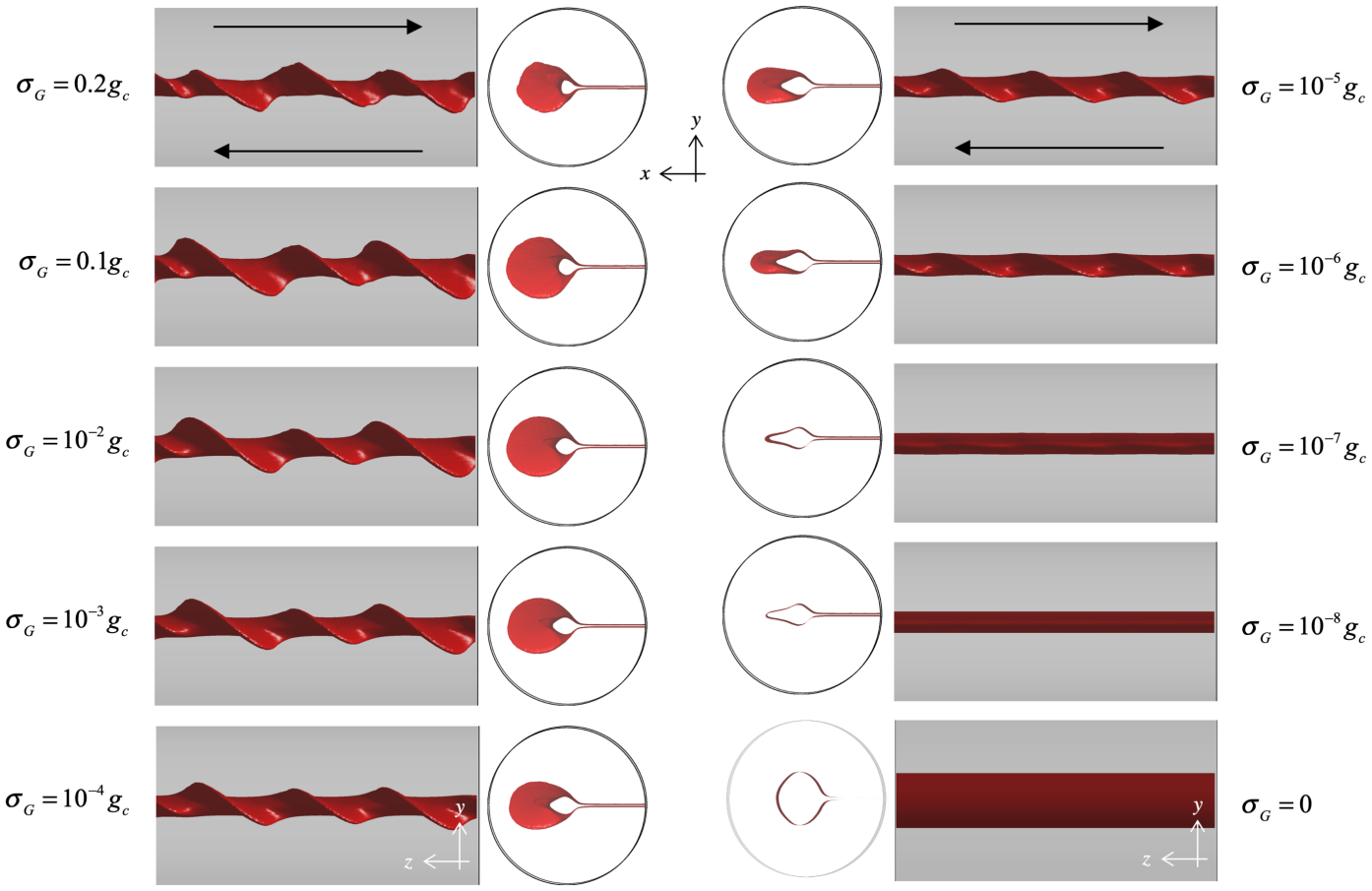

Figure A.21: Effect of variation in fracture toughness (σ_G) on the crack pattern for the same loading.

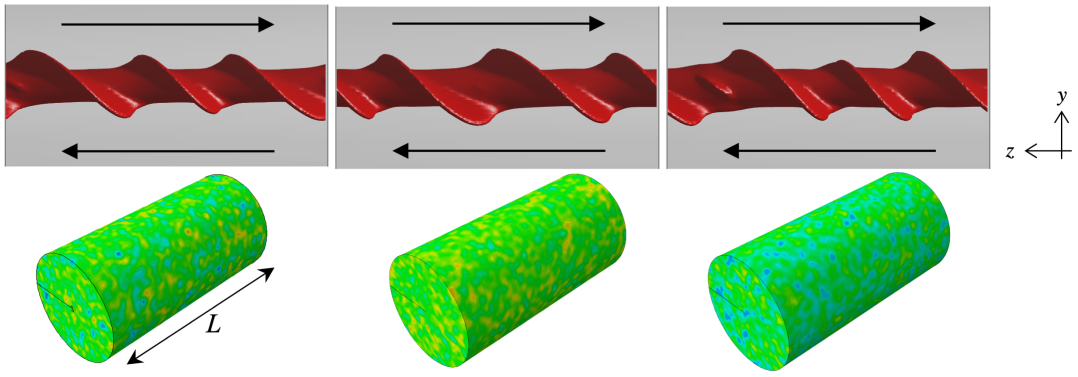

Figure A.22: Effect of different random g_c distributions on the crack pattern.

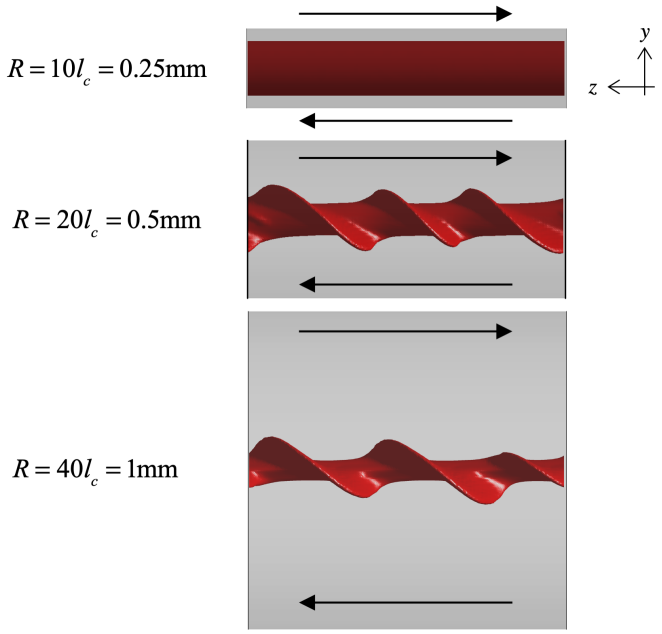

Figure A.23: Effect of model size R on the crack pattern.

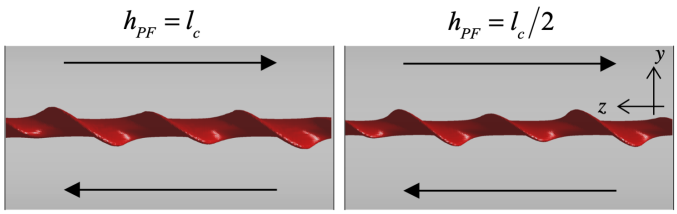

Figure A.24: Effect of finite element mesh size on the crack pattern.

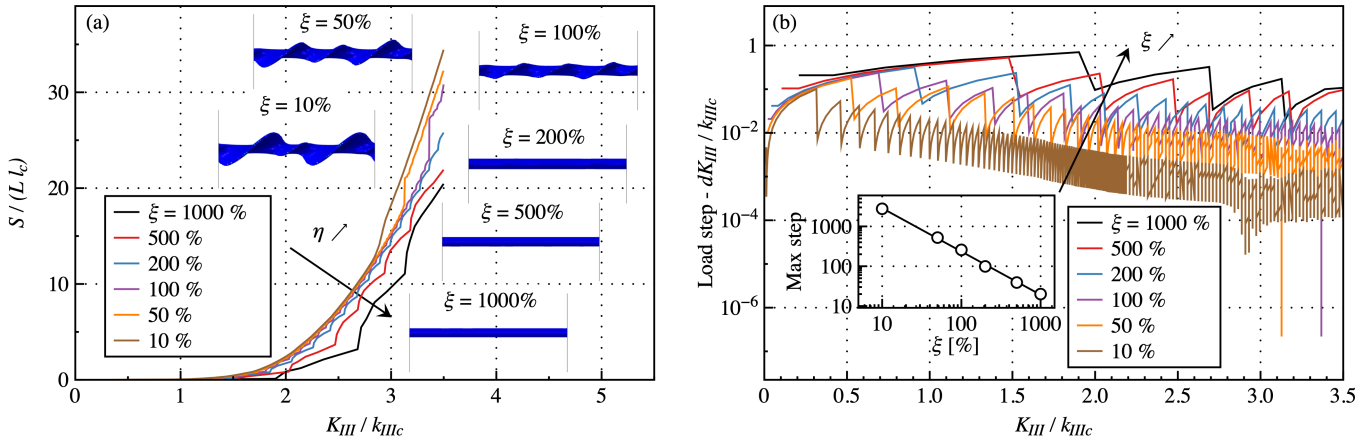

Figure A.25: Impact of load step control on (a) crack pattern and (b) load step. The inset displays the iterations required to achieve $K_{\mathrm{III}}/k_{\mathrm{IIIc}} = 2.54$.

The load increments were determined by an automated algorithm governing the local crack driving energy density increment, as detailed in previous work of Molnár et al. (2020a) and Molnár et al. (2022):

$$\max(d\psi_0^+) = \xi \frac{3g_c}{8l_c}, \tag{A.1}$$

Here, ξ served as a scalar parameter dictating the calculations precision. Smaller values resulted in finer load steps and a more precise iteration. Fig. A.25a illustrates the crack surface evolution with loading for different ξ values. Initial localizations were discernible at $\xi = 100\%$, while they became well-defined at $\xi = 50\%$.

Additionally, Fig. A.25b portrays the load step evolution during the calculation for varying ξ values. The load step consistently diminishes with decreasing ξ and increasing loading. Minor fluctuations stem from the automatic step control inherent in the software employed.

Appendix B. Supplementary Material

The supplementary material includes two files: "CrackCoarsening.mp4" and "MODE3.zip". The file "CrackCoarsening.mp4" is a video showcasing the initiation, propagation, and arrest of crack facets in a large-scale model with parameters $R = 40l_c$, $L = 200l_c$, and $\nu = 0$.

On the other hand, the file "MODE3.zip" contains a small working example of our model. To launch the example, the following command should be used:

```
abaqus job=MODE3 input=MODE3.inp user=MODE3.f interactive
```